NTNU
Norwegian University of
Science and Technology

Computational Diagnosis of Coronary Artery Disease

A comparison of steady and transient blood flow simulations for FFR

Simen Aamodt

Mechanical Engineering	
Submission date:	June 2017
Supervisor:	Leif Rune Hellevik, KT
Co-supervisor:	Lucas Omar Müller, KT

Norwegian University of Science and Technology
Department of Structural Engineering

ACCESSIBILITY
Open

Department of Structural Engineering
Faculty of Engineering Science and Technology
NTNU- Norwegian University of Science and Technology

MASTER THESIS 2017

SUBJECT AREA: Applied Mechanics (Biomechanics)	DATE: 11.06.17	NO. OF PAGES: 97

TITLE:

Computational Diagnosis of Coronary Artery Disease
A comparison of steady and transient blood flow simulations for FFR

BY:

Simen Aamodt

SUMMARY:

An emerging method for non-invasive diagnosis of coronary artery disease is the computational assessment of fractional flow reserve (FFR), a patient normalized physiological index quantifying arterial pressure drop. Computational FFR (FFR_{CT}) is assessed through combining CT-images with fluid dynamics simulations. To reduce the complexity of computational models and related cost, it is desirable to validate the assumption of quasi-steady behavior of coronary blood flows.

The present work was incorporated in the development of models and methods in NTNU's research project on FFR_{CT} . Computational fluid dynamics (CFD) simulations were used in the validation of a coupled 3D-0D model for coronary circulation. The model was further used in patient-specific simulations tailored to the data from 8 patients recruited at St. Olavs Hospital, Trondheim. Steady and transient blood flow simulations were compared to evaluate the implications of neglecting pulsatility in the calculation of FFR_{CT}.

The results demonstrate that assuming steady flow conditions introduce negligible errors compared with other model errors and the variations in repeated invasive FFR procedures. The FFR_{CT} results obtained with the present methodology and models are promising, yet with occasionally severe errors in per-patient comparison with invasive FFR. Further development of models and methods is required for adequacy in diagnostic applications.

SUPERVISOR(S): Leif Rune Hellevik, Lucas Omar Müller

CARRIED OUT AT: NTNU

Acknowledgments

First of all, I would like to thank my advisor, professor Leif Rune Hellevik, for strong and helpful guidance throughout the whole project. He has been remarkable in connecting me with the right people, and continuously coming with suggestions for my work. I would like to express my deepest gratitude to my co-advisor, post doctor Lucas Omar Müller. Without his help with implementation of computational models, discussions on physiological and numerical topics, providing me with his own computational resources for my simulations, giving me feedback on this thesis, and general guidance, the outcome of this project would most certainly have been of lower quality. I would also like to thank Ph.D. candidate Fredrik Eikeland Fossan for offering me his help with everything from installation of software, to segmentation of coronary arteries, to valuable discussions, and giving feedback on this thesis. The clinicians at St. Olavs Hospital have been very helpful by inviting me to participate in clinical procedures for CT imaging, and answering my narrow-minded engineering questions. Thanks to my friends Mathias Stensland Lillevold and M.D. Anders Einum for inspirational late-lunch and mid-run discussions, and thanks to former classmates Johannes Kløve Kjernlie and Hallvard Moian Nydal for help with the thesis layout. Finally, I would like to thank all friends and family being supportive throughout the work with this project.

Preface

This master's thesis is the culmination of a Master of Science degree in Mechanical Engineering at the Norwegian University of Science and Technology (NTNU). The master's project has been conducted in relation to an ongoing research project in the Division of Biomechanics at the Department of Structural Engineering, and represents partial fulfillment of a specialization in Applied Mechanics.

What do you find when you look really deep into someones heart? Love? Compassion? Atherosclerotic plaque? I have spent the last six months looking into people's hearts. And here is what I have found: An indomitable desire to learn about the governing principles of nature. An exquisite excitement about the entanglement of multiple branches in science and art. A passion for the fascinating interrelatedness of physical concepts. And finally, a curiosity probably also inspiring one of the first persons to really scrutinize hearts, the pioneer of cardiovascular research, Leonardo da Vinci. Although this thesis will not even contribute a millionth of a fraction as much as his pioneering work, I am certain that I have experienced some of the same enthusiasm he did 500 years ago. I am truly grateful for having been given the opportunity to explore this field of science, where medicine meets engineering.

Simen Aamodt

Simen Aamodt
June 11, 2017

Assignment

Measuring the fractional flow reserve (FFR) is the current gold standard for diagnosis of stable coronary artery disease. Traditional invasive procedures to measure arterial pressure drop, and per se FFR, constitute a major consumer of scarce healthcare resources for a group of diseases rapidly increasing in incidence. As a consequence, non-invasive diagnosis using CT images and computational fluid dynamics (CFD) simulations is emerging as a cost-effective and risk-reducing alternative to traditional methods. However, these techniques are affiliated with the solving of complex mathematical models requiring extensive computational power. The feasibility of computational FFR (FFR_{CT}) in clinical applications relies on the development of accurate and computationally effective models.

A considerate amount of the computational expense is associated with the discretization of the pulsatile nature of coronary flow. Based on the fact that FFR is a time averaged quantity, stationary flow simulations of time averaged conditions have become increasingly popular in the methodology of several research groups working on FFR_{CT}. However, there is a cavity in research of questioning the significance of the steadiness assumption. For the development of models to be applied in NTNU's FFR_{CT} project, it is desirable to investigate the effect of assuming steady conditions. The master's project will investigate the effect of the steadiness assumption, with the main objective being

- Determine the importance of pulsatility in flow simulations for the assessment of FFR_{CT}

In the work with this objective, it is expected that the work would include the following tasks

- Contribute to the development of a methodology for calculations of $\mathrm{FFR}_{\mathrm{CT}}$
- Make patient-specific models for coronary flow simulations
- Perform steady and unsteady CFD simulations and compare the results

A master's thesis is to be submitted in partial fulfillment of a Master of Science degree in the field Applied Mechanics at the Department of Structural Engineering, NTNU. The project is credited 30 ECTS in the course TKT4915 - Computational Mechanics.

Thesis supervisor: Leif Rune Hellevik
Co-supervisor: Lucas Omar Müller
Simen Aamodt

COMPUTATIONAL DIAGNOSIS OF CORONARY ARTERY DISEASE

A comparison of steady and transient blood flow simulations for FFR

ABSTRACT

An emerging method for non-invasive diagnosis of coronary artery disease is the computational assessment of fractional flow reserve (FFR), a patient normalized physiological index quantifying arterial pressure drop. Computational FFR ($\mathrm{FFR}_{\mathrm{CT}}$) is assessed through combining CT images with fluid dynamics simulations. To improve feasibility of such methods for clinical use, it is desirable to validate the assumption of quasi-steady behavior of coronary blood flows.

The present work was incorporated in the development of models and methods in NTNU's research project on $\mathrm{FFR}_{\mathrm{CT}}$. Computational fluid dynamics (CFD) simulations were used in the validation of a coupled 3D-0D model for coronary circulation. The model was further used in patient-specific simulations tailored to the data from 8 patients recruited at St. Olavs Hospital, Trondheim. Steady and transient blood flow simulations were compared to evaluate the implications of neglecting pulsatility in the calculation of $\mathrm{FFR}_{\mathrm{CT}}$.

The results demonstrate that assuming steady flow conditions introduce negligible errors compared with other model errors and the variations in repeated invasive FFR procedures. The $\mathrm{FFR}_{\mathrm{CT}}$ results obtained with the present methodology and models are promising, yet with occasionally severe errors in per-patient comparison with invasive FFR. Further development of models and methods is required for adequacy in diagnostic applications.

Veileder: Leif Rune Hellevik
Medveileder: Lucas Omar Müller
Simen Aamodt

BEREGNINGSBASERT DIAGNOSTISERING AV KORONARSYKDOM

En sammenligning av stasjonære og transiente strømningssimuleringer

SAMMENDRAG

FFR er en pasientnormalisert, fysiologisk indeks for diagnostisering av koronarsykdom, basert på trykkfall i koronararteriene. Fluiddynamiske simuleringer av blodstrømning kan brukes til å anslå FFR ikke-invasivt, men er assosiert med beregninger som stiller store krav til regnekraft. For å øke anvendeligheten av slike metoder er det ønskelig å undersøke effekten av å anta stasjonære strømningsforhold i simuleringer, som et alternativ til transiente.

Arbeidet i denne oppgaven har vært knyttet til utvikling av modeller og metoder i NTNUs forskningsprosjekt på $\mathrm{FFR_{CT}}$. Numeriske strømningssimuleringer (CFD) har blitt brukt i valideringen av en koblet 3D-0D beregningsmodell for koronarstrømning. Modellen ble videre brukt i pasientspesifikke simuleringer tilpasset data fra 8 pasienter rekruttert ved St. Olavs Hospital. Stasjonære og transiente simuleringer ble sammenlignet for å vurdere konsekvensen av å anta stasjonære forhold i beregninger av $\mathrm{FFR_{CT}}$.

Resultatene viser at forskjellen mellom stasjonære og transiente simuleringer er neglisjerbar sammenlignet med andre modellfeil og variasjon i invasive FFR-målinger. Selv om beregningene av FFR i enkelte tilfeller treffer bra ved sammenligning med invasive målinger, kreves det mer utvikling av modellene og metodene som er brukt før de kan brukes i kliniske anvendelser.

Contents

List of Tables

List of Figures

Acronyms

CA Coronary Artery

CAD Coronary Artery Disease

CCTA Cardiac Computed Tomography Angiography

CFD Computational Fluid Dynamics

CO Cardiac Output

CT Computed Tomography

DBP Diastolic Blood Pressure

FEM Finite Element Methods

FFR Fractional Flow Reserve

FFR$_{CT}$ Computational Fractional Flow Reserve

HR Heart Rate

ICA Invasive Coronary Angiography

IPCS Incremental Pressure Correction Scheme

LAD Left Anterior Descending Coronary Branch

LCA Left Coronary Artery

LCX Left Circumflex Coronary Branch

LM Left Main Coronary Branch

LV Left Ventricle

MAE Mean Absolute Error

MAP Mean Arterial Blood Pressure

N-S Navier-Stokes (equations)

PDE Partial Differential Equation

PP Pulse Pressure

RCA Right Coronary Artery

RMSE Root Mean Square Error

SBP Systolic Blood Pressure

1

Introduction

Cardiovascular diseases constitute a major healthcare challenge in the world. With more than 17 million deaths each year it has the highest mortality rate in the world, and numbers are expected to increase considerably the coming years [1]. Nearly half of the deaths are caused by coronary artery disease (CAD) [2], a group of diseases already requiring substantial clinical resources for treatment and diagnosis. Invasive pressure measurements to determine the fractional flow reserve (FFR) has established as the leading procedure for diagnosis of stable CAD. Despite being superior to alternatives in both cost [3–5] and reliability [6–8], its effectiveness is disputable due to a high rate of negative diagnosis results [9].

In the emerging field of personalized medicine, novel techniques exploiting the latest developments in medical imaging, computer science and fluid dynamics are challenging conventional methods to derive FFR. Non-invasive diagnosis of CAD based on physical calculations is on the verge of altering the current paradigm of clinical diagnostics, by the use of sophisticated computer simulations of blood flow on patient-specific models.

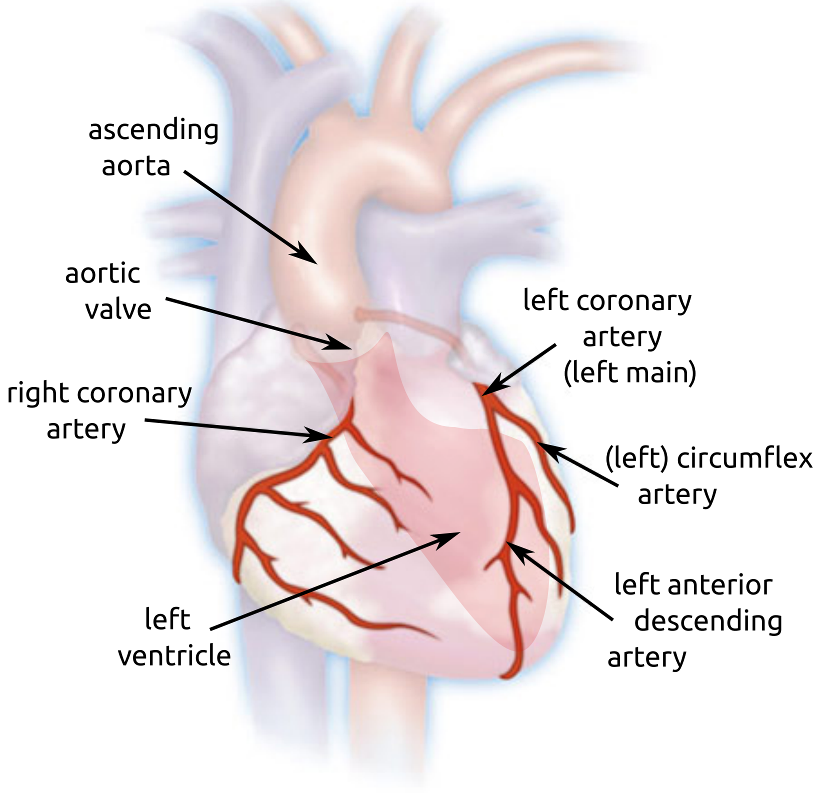

Figure 1.0.1: Anatomy of the coronary arteries [10].

1.1 Coronary Artery Disease

The coronary arteries (CAs) constitute the oxygen supply network for the heart muscle. The two main branches, the right coronary artery (RCA) and left coronary artery (LCA), branch off the ascending aorta immediately after the aortic valve, and propagate into the heart walls to ensure blood perfusion the the vast majority of the heart muscle tissue (myocardium). In the left coronary tree, the left main (LM) artery bifurcate into the left anterior descending (LAD) and the left circumflex (LCX) arteries, further subdividing until reaching the level of arterioles.

Coronary artery disease (CAD) is signified by insufficient oxygen supply to the myocardium. The most common symptom of CAD is chest pain (angina pectoris), usually increasing in intensity with exercise. CAD is caused by narrowing or stiffening of the CAs, limiting their abilities to transport blood effectively. Such conditions are predominantly caused by atherosclerosis, the deposition of cholesterol on the inner vessel walls (endothelium), gradually being calcified to atherosclerotic plaque [11]. Ischeamia is the condition of degradation of the myocardium caused by scarcity of oxygen. If untreated, ischaemia may ultimately lead to heart attack (myocardial infarction), and in severe cases heart failure and death [12].

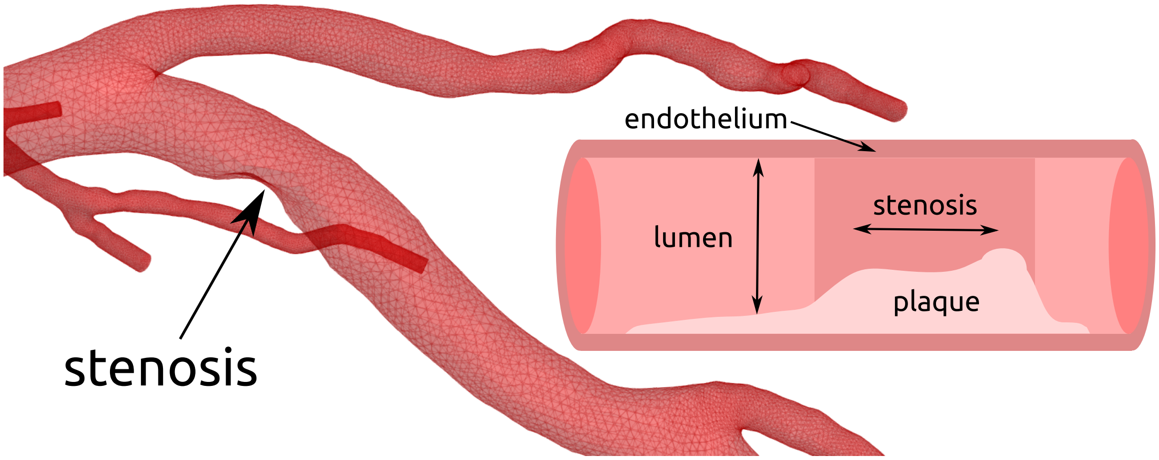

Figure 1.1.1: 3D model of a lumen segment of a coronary tree, with an illustration of a stenosed artery.

1.2 DIAGNOSIS OF CORONARY ARTERY DISEASE

Diagnosis of stable CAD relies on the clinical assessment of the functional severity of stenoses[1] in the CAs, i.e. their significance in obstructing the blood flow. A patient-specific physiological index called the fractional flow reserve (FFR) has emerged as the gold standard for evaluation of CA stenoses [6, 7]. FFR is (by the clinical definition) the ratio of the cardiac cycle average pressures downstream (distal) and upstream (proximal) of the stenosis.

$$FFR = \frac{P_d}{P_p} \tag{1.1}$$

---

[1] Stenosis: A narrowing section of an artery.

Pressures can be measured in patients by catheterization, through a clinical procedure called invasive coronary angiography (ICA). The pressures are measured at specific locations in the CAs by using a pressure sensor attached to a guidewire. An FFR-value of less than 0.75 will require further intervention, as the risk of severe events due to ischaemia is significant [7]. In clinical studies and diagnosis, a cut-off value of 0.80 is common [6, 8].

CAD is a major health problem, being the group of cardiovascular diseases that takes the most lives each year [2]. Better treatment and diagnosis of CAD is essential to overcome the expected increase in CAD related deaths. Although FFR measured *in vivo* is diagnostically accurate, it is ineffective to perform ICAs on all angina patients, as negative tests have high occurrence. In 2013, the *PLATFORM* study reported that among ICAs on 187 suspected CAD patients, there were only found obstructive lesions in 27% [9]. It lays a great potential in reducing the number negative ICAs, to reduce the occupation of clinical resources and to avoid unnecessary risk for patients.

1.3 COMPUTATIONAL FFR

An emerging method for determining FFR is through calculations instead of measurements, assessing the computational FFR (FFR_{CT}). Fluid mechanical theory is applied to simulate the blood flow in the CAs to compute the stenotic pressure drops, and per se FFR. By the use of computational fluid dynamics (CFD), the diagnosis process may elude invasive procedures, for the benefit of the patients as well as health institutions. Hlatky et al. reported that FFR_{CT} could reduce costs by 30% when used to guide medical intervention procedures, and a 12% reduction in events post-diagnosis [5]. These findings are supported by several other studies [3, 4, 9].

When computing FFR_{CT}, a CT scan of the patient's heart can be used to extract the 3D geometry of the CA blood flow domain (lumen), a process called segmentation. The 3D model is then subjected to the required steps to solve the fluid mechanical equations and obtain the CFD results for pressure and flow. Relevant patient-specific measurements are incorporated in the computations to assure similarity with the real blood flow. Finally, the results are post-processed in order to obtain the estimated FFR-values at the relevant locations in the CAs.

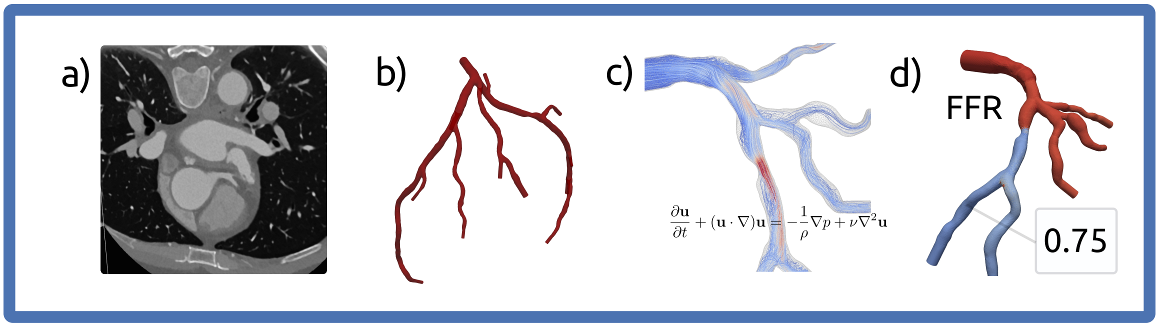

Figure 1.3.1: Workflow for noninvasive computation of $\mathrm{FFR}_{\mathrm{CT}}$: a) Cardiac computed tomography angiography (CCTA) of a patient's heart, b) 3D segmentation of the coronary arteries, c) CFD simulations of the flow, and d) $\mathrm{FFR}_{\mathrm{CT}}$ results for the coronary arteries.

1.3.1 PREVIOUS WORK ON $\mathrm{FFR}_{\mathrm{CT}}$

The application of patient-specific mathematical modeling has already proven to be valuable both for diagnostics and in virtual assessment of individual treatments [9, 13]. Recent developments in imaging and computer technology are contributing to the feasibility of highly sophisticated computations in clinical procedures.

Several research communities around the world aim at solving the challenges with *in silico*[2] assessment of FFR. Among the most successful are Stanford University-based HeartFlow, Inc., receiving FDA[3] approval for their $\mathrm{FFR}_{\mathrm{CT}}$ software as a commercial diagnostic tool to be used in clinical procedures. They also achieved a position among the top 15 healthcare deals of 2016, after raising almost $100M in fundings [14]. However, there are still challenges to overcome to enhance the feasibility and accuracy of $\mathrm{FFR}_{\mathrm{CT}}$ methods. In the HeartFlow NXT trial results [15], $\mathrm{FFR}_{\mathrm{CT}}$ had a probability of detection (sensitivity) of 86% for lesions with $\mathrm{FFR}<0.8$. It is especially desirable to increase the sensitivity, as the success of a diagnostic procedure relies heavily on the ability to avoid false negatives.

Morris et al. from the University of Sheffield has developed methods and models achieving 97% accuracy in signifying severe lesions in 35 patients [16]. However, their models are based on input from invasive measurements, and computations require 12-24 hours of run time, which is impractical in clinical applications. A considerate amount of the computational cost is associated

---

[2] In silico: From latin, ”in computer” or ”via computer simulations”.

[3] FDA: U.S. Food and Drug Administration

with simulating the pulsatility in coronary flows. Thus, some researchers have approached $\mathrm{FFR}_{\mathrm{CT}}$ with stationary models, only accounting for the averages of pressure and flow over the cardiac cycle.

Tu et al. have reported to simulate steady 3D coronary flows in 5 minutes [17], identifying severe stenoses with an accuracy of 88%. They do not discuss whether the steadiness condition may contribute significantly to the errors in FFR. Zhang et al. [18] also assess time-averaged flows, with a sensitivity of 80%. They argue that steady state is a limitation when transient pressure waveforms are of interest. However, they do not discuss the significance of assuming stationary flow for the prediction of FFR.

Although both unsteady and steady computations are well established in concurrent $\mathrm{FFR}_{\mathrm{CT}}$-methodologies, none of the aforementioned studies verifies their choice of inclusion or exclusion of pulsatility in their models. A study by Huo et al. have investigated the importance of unsteadiness in *in vitro* experiments, concluding little significance to time average pressure drop across a stenosis [19]. In similar experiments, Mates et al. report of quasi-steady behavior of stenotic coronary flows [20].

There is a very limited basis in previous studies on $\mathrm{FFR}_{\mathrm{CT}}$ to confirm that these findings also apply for CFD simulations. One study by Bulant et al. published previously this year [21] visits the comparison of steady and transient simulations, reporting small deviations in computed $\mathrm{FFR}_{\mathrm{CT}}$. Except from these results, there are no publications known to the author that are fully dedicated to question the significance of the steadiness assumption in CFD simulations for the assessment of FFR.

1.4 THESIS OBJECTIVES

When reducing complex computational models it is crucial to justify the assumptions made, and to verify that the consequent errors are negligible. In the development of the methodology for the FFR_{CT}-project at NTNU[4], one of the main goals is to achieve accurate FFR_{CT} computations at low computational expenses. This thesis aims at comparing steady and transient flow simulations for derivation of FFR_{CT}, with the main objective being:

- Determine the significance of errors introduced by assuming steady flow conditions in CFD simulations for the assessment of FFR_{CT}

In order to achieve this, it is expected that the following single objectives should be met:

- Contribute to the development of a methodology for calculations of FFR_{CT}
- Validate a computational model for numerical simulations of patient-specific coronary flows
- Perform steady and unsteady 3D CFD simulations and compare the results

1.5 OUTLINE

The rest of this thesis is structured in five chapters. Chapter 2 is a collection of theoretical topics from fields of relevance to the subsequent chapters. In chapter 3, the methods and computational models developed and applied in the work is presented in detail. Chapter 4 presents the results from the generation of patient-specific models and the CFD simulations. A comprehensive discussion of the methods and results is arranged in chapter 5. Finally, the thesis is recapitulated in chapter 6 through a summary of the work and the final conclusions from the discussion.

---

[4] *NTNU's FFR_{CT}-project: "Model based, non-invasive diagnosis of coronary artery disease with 3D ultrasound and CT"*

2

Theoretical Background

This chapter contains a selection of theoretical topics of relevance to $\mathrm{FFR}_{\mathrm{CT}}$ computations. Computational biomechanics is a multidisciplinary field, and the modeling of coronary flow is no exception. Medicine, imaging technology, mathematics, chemistry, mechanics, computer technology, fluid dynamics and biology are just some of the professions being absorbed in the development of non-invasive FFR methods.

For the limited extent of this thesis, this chapter is confined to include a selection of theoretical topics relevant for the discussion of the applied methods and the results obtained in this work. In the first section, the physiology of the coronary arteries is presented, focusing on the underlying mechanisms governing coronary flow. Secondly, fundamental fluid mechanics theory and basic CFD methodology are presented. In the last section, the intersecting field of physiology and fluid mechanics is presented through the mathematical modeling principles of coronary flows.

2.1 CORONARY BLOOD FLOW

As stated in the introduction, the coronary arteries are supplying the myocardium with oxygenated blood. During systole, the ejection phase of the heart, blood is pumped out from the left ventricle (LV) through the aortic valve and into the ascending aorta, where the CAs branch off (figure 2.1.1). The most characteristic feature distinguishing coronary blood flow from other cardiovascular flows is the suppressed blood flow during systole [22]. Due to the contraction of the myocardium, tissue pressure increase the back pressure on the distal CAs, resulting in an increased resistance to flow [12]. As a consequence coronary flow is maximal during diastole, the relaxation phase of the cardiac cycle. This pattern is more prominent in the LCA than in the RCA due to the proximity of the LV (the systolic pressure in the right ventricle (RV) is considerably lower than in the LV) [11].

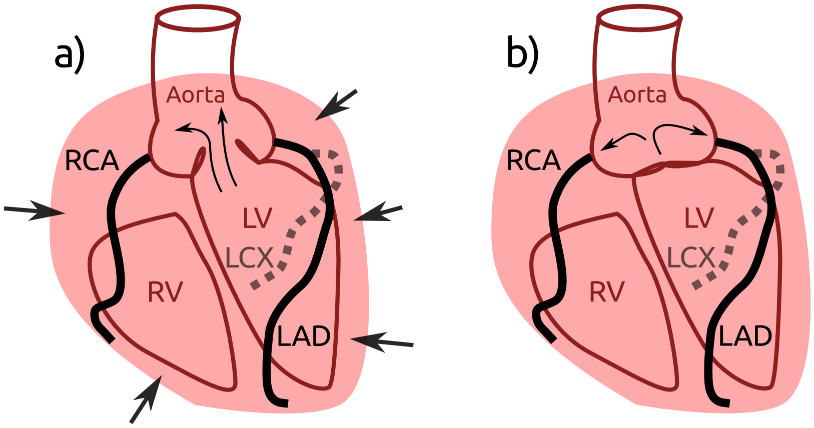

Figure 2.1.1: Flow in the coronary arteries: a) flow is limited during systole and b) increased coronary flow during diastole.

2.1.1 RESISTANCE TO FLOW

The driving force of coronary flow is the pressure in the ascending aorta. When this pressure exceeds the opposing pressure from the distal and peripheral parts of the CAs, coronary flow is positive. In general, the resistance to flow in the human arterial tree is located in the arterioles [23], with the contribution from large, conduit CAs being negligible under normal circumstances [12]. However, when a stenosis is present resistance in the larger vessels become significant. Based on *in vitro* experiments, Young and Tsai [24] proposed a formulae for the pressure drop across a stenosis,

$$\Delta P_{stenosis} = \frac{K_v}{Re_D}\rho u^2 + \frac{K_t}{2}\left(\frac{A_0}{A_s} - 1\right)^2 \rho u^2, \tag{2.1}$$

where A_0 and A_s are the original and stenosed cross-sectional lumen area respectively, and ρ is the density of the blood. u is the mean velocity in the unobstructed part of the vessel, and Re_D is the Reynolds number (to be defined in 2.2.3). K_v and K_t are constants being dependent upon the geometry and severity of the stenosis. For a given flow rate Q, equation (2.1) becomes

$$\Delta P_{stenosis} = \frac{K_v \mu}{A_0 D_0} Q + \frac{K_t \rho}{2{A_0}^2}\left(\frac{A_0}{A_s} - 1\right)^2 Q^2 = a_1 Q + a_2 Q^2, \tag{2.2}$$

where D_0 is the original lumen diameter and μ is the dynamic viscosity of blood. The first term is associated with the viscous friction loss due to the contraction of the vessel. The second term rise from separation of the flow in the expanding region of the stenosis, where pressure drop is proportional to the square of the flow rate [23].

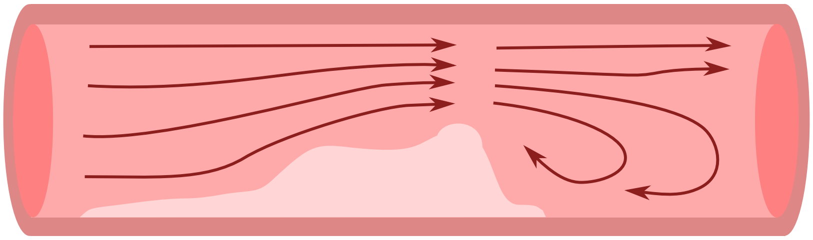

Figure 2.1.2: Illustration of streamlines through a stenotis. The pressure drop in the narrowing section of the stenosis is proportional to the flow, while the separation of flow in the expansion generates a pressure drop proportional to the flow rate squared.

2.1.2 BASELINE CONDITIONS

Baseline, or resting coronary flow rate is approximately 4-5 percent of the total cardiac output (CO), on average ∼225 ml/min [11]. The distribution of flow between the LAD and RCA depends on the physiology of the coronary tree, which can be left or right dominant. About 60 percent of the coronary flow runs through the LCAs (LAD and LCX) in a right (sic) dominant coronary tree, prevailing in approximately 90 percent of the cases [25]. In the opposite case, the LCA flow is almost 80 percent of the coronary flow.

2.1.3 HYPEREMIA

Hyperemia, the state of maximal coronary flow, is the natural response to increased oxygen demand by the myocardium. Blood flow increases primarily as a result of arteriolar vasodilation, autoregulated expansion of the coronary arterioles decreasing the peripheral resistance [11]. During hyperemia, the main contribution to the coronary resistance is redistributed from the arterioles to the capillaries [26]. For clinical procedures, hyperemia can be provoked through exercise or the use of pharmacologic agents.

Adenosine is a common agent used when measuring FFR invasively. The individual response to adenosine is varied, making it difficult to predict hyperemic flow rates from baseline conditions. Hyperemic coronary blood flow as a response to adenosine is 2 to 5 times of the basal flow rate [27–29]. Aortic pressure and heart rate (HR) is mildly affected by adenosine. An insignificant or small (5-16 *mmHg*) decrease in mean arterial blood pressure (MAP), and small to moderate increase in HR by 15-20% has been observed in different studies [27, 29, 30].

2.1.4 FRACTIONAL FLOW RESERVE

The fractional flow reserve (FFR) is used by physicians to assess the functional severity of a stenosis. It is derived from the ratio of the actual flow in a stenosed vessel to the hypothetical flow if the vessel had no stenosis (2.3).

$$FFR = \frac{Q_s}{Q_h} \tag{2.3}$$

With negligible assumptions, this equals the ratio of pressure distal and proximal to the stenosis [23]:

$$FFR = \frac{P_d}{P_p} \tag{2.4}$$

FFR is a time averaged quantity, defined by the mean pressures over one cardiac cycle. The derivation of equation (2.4) from (2.3) is visited in appendix A. Since pressure drops in the large, unobstructed vessels are negligible, it is common practice to use the aortic pressure as P_p in equation (2.4).

2.2 FLUID MECHANICS

The study of the mechanics of fluids has occupied scientists' attention for thousands of years. The progress has evolved from the calculation of buoyancy forces in ancient Greece, to the state-of-the-art computations of turbulence in supercomputers. In the perpetual search for comprehension of the nature, the exquisite behavior of fluids never seem to temper the human curiosity.

2.2.1 GOVERNING EQUATIONS

The contemporary paradigm for mathematical description of continuous fluid motion is by the Navier[1]-Stokes[2] (N-S) equations. Although the theoretical foundation was established early in the 19th century, a complete understanding of its nature and behavior remains one of the greatest challenges in physics and mathematics [33]. The N-S equation is Newton's 2nd law expressed for fluids, or the balance of the rate of change of momentum with fluid forces. As conservation of mass is required to completely describe the fluid motion, the N-S equations often refer to both the momentum equations and the continuity equation in CFD-terminology. For an incompressible, Newtonian fluid[3], the N-S equations (with continuity) on conservation form are [34]:

$$\frac{\partial \mathbf{u}}{\partial t} + (\mathbf{u} \cdot \boldsymbol{\nabla})\mathbf{u} = -\frac{1}{\rho}\boldsymbol{\nabla} P + \nu \boldsymbol{\nabla}^2 \mathbf{u} \tag{2.5a}$$

$$\boldsymbol{\nabla} \cdot \mathbf{u} = 0 \tag{2.5b}$$

Equation (2.5a) is the vector equation containing three equations for balance of momentum in 3 dimensions, and equation (2.5b) expresses conservation of mass (or divergence-free flow for an incompressible fluid). $\mathbf{u}$ is the velocity vector, P is the pressure, and t is time. ρ and ν are material constants of the fluid, density and kinematic viscosity respectively. $\boldsymbol{\nabla}$ is the del operator in three dimensions, and $\boldsymbol{\nabla}^2 = \boldsymbol{\nabla} \cdot \boldsymbol{\nabla}$.

In the momentum equation, the left-hand-side terms are associated with acceleration of the fluid, transient and spatial respectively. On the right-hand-side, the first term represents the pres-

---

[1] Claude-Louis Navier (1785-1836), French engineer and physicist [31]

[2] Sir George Gabriel Stokes, 1st Baronet (1819-1903), physicist and mathematician from Ireland [32].

[3] Newtonian fluid: A fluid in which the viscous stresses are linearly proportional to the strain rate.

sure forces (opposing the flow as convention), and the second term the viscous forces. To adequately define a fluid flow problem, equation (2.5) has to be combined with initial and boundary conditions. Boundary conditions (BCs) are commonly prescribed either in terms of the value of a field variable on the boundary (Dirichlet BCs), or the value of its normal gradient across the boundary (Neumann BCs).

The incompressible N-S equations is an example of a hyperbolic-parabolic system of partial differential equations (PDEs). Analytical solutions of (2.5) are only obtainable for very simple boundary conditions and geometrical configurations. For practical problems, solving of the N-S equations requires either making simplifying assumptions about the physical problem or solving the equations numerically.

Internal pipe flow is a special case of fluid mechanical problems. The Poiseuille[4] solution is an analytical solution of the N-S equations for simple flows in pipes of constant, circular cross-sections. Assuming rigid walls and steady, laminar flow, Poiseuille's equation for the velocity profile is

$$u(r) = \frac{r_l^2}{4\mu}\frac{dP}{dx}\left(1 - \left(\frac{r}{r_l}\right)^2\right) \tag{2.6}$$

In equation (2.6), $\mu = \nu/\rho$ is the dynamic viscosity, and r_l is the radius of the lumen cross-section. r is the radial coordinate from the center of the tube, and x is the longitudinal coordinate. Evidently, the velocity profile according to equation (2.6) is parabolic. Integrating equation (2.6) over the cross-section yields in the expression for volumetric flow rate:

$$Q = \frac{\pi r_l^4}{8\mu}\frac{dP}{dx} \tag{2.7}$$

For situations where the assumption of rigid, straight tubes with steady flow conditions cannot be justified, equations (2.6) and (2.7) are inadequate. In such situations the N-S equations can be solved numerically, applying methods from the field of fluid mechanics called computational fluid dynamics (CFD).

---

[4] Jean Léonard Marie Poiseuille (1797-1869), French physicist and physiologist [35].

2.2.2 COMPUTATIONAL FLUID DYNAMICS

It is presently not known whether smooth solutions to the N-S equations always exist [33]. Nevertheless, considerate research in the validation of numerical solution algorithms have ensured the establishment of CFD as an indispensable tool on the frontiers of modern fluid mechanics.

FINITE ELEMENT METHODS FOR FLUID PROBLEMS

Several methods are available to solve the Navier-Stokes equations numerically. The most commonly applied methods can be divided into three groups: finite difference methods (FDM), finite volume methods (FVM) and finite element methods (FEM). They all represent numerical methods as mathematical tools to solve physical problems modeled by PDEs. For all three groups, the PDEs are discretized in time and space. Since FEM are employed in the present work, these are given the most attention in the following.

In the FEM for fluid dynamics, the N-dimensional spatial domain containing the fluid is partitioned into a finite number of regularly shaped elements. Examples of 2D triangular elements are shown in figure 2.2.1. Each element is equipped with a set of interpolation functions, e.g. linear or quadratic, determining the order of the element. These functions are used to represent the field variables, such as pressure and flow, within the element as functions of the element nodal values.

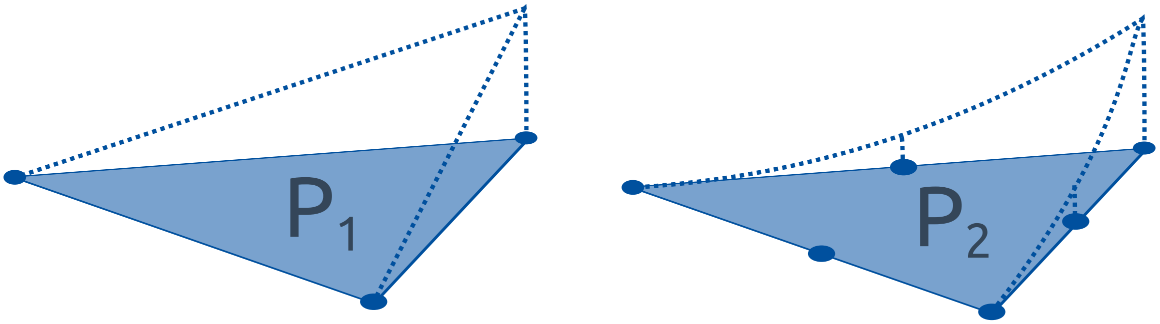

Figure 2.2.1: Two simple triangular 2D elements, the Lagrange P_1 with linear interpolation functions, and P_2 with quadratic. 3D tetrahedral elements can consist of four faces of these elements.

The FEM approach the physical problem through the weak form representation of the governing differential equations [36]. The weak form of an equation is obtained by multiplying its variables by arbitrary weighting functions ($\mathbf{w}$) before integrating over the domain (Ω), and thus reducing the degrees of the derivatives. The N-S (momentum) equations on weak form are shown in equation (2.8), assuming zero boundary integrals and applying the divergence theorem on the pressure and viscous terms [34].

$$\int_\Omega \mathbf{w} \cdot \frac{\partial \mathbf{u}}{\partial t} d\Omega + \int_\Omega \mathbf{w} \cdot (\mathbf{u} \cdot \boldsymbol{\nabla})\mathbf{u} d\Omega + \int_\Omega \frac{P}{\rho} \boldsymbol{\nabla} \cdot \mathbf{w} d\Omega + \int_\Omega \boldsymbol{\nabla}\mathbf{w} : \nu \boldsymbol{\nabla}\mathbf{u} d\Omega = 0 \tag{2.8}$$

The FEM seeks to solve what is called the *weak formulation* of the PDEs. Avoiding the mathematical stringency, the weak formulation of (2.8) can be expressed simplified as *"find* **u** *on the function space* **V** *such that (2.8) is satisfied"* [37]. A discrete FEM function space **V** consists of the union of the interpolation (or shape) functions of all elements. If the function space is not discrete, but contains infinitely many functions, solving the weak formulation gives the exact solution of (2.8) [34].

The non-linearity of the N-S equations makes it difficult to solve even in its weak formulation. Several different methods exist for linearizing equation (2.5), and many rely on the splitting of pressure and velocity in the equations [34]. One such scheme is the incremental pressure correction scheme (IPCS), which has shown good efficiency in comparison with alternative schemes [38]. Discretizing the N-S equations with the implicit Euler method in time, and linearizing the non-linear convection term as $\mathbf{u}^{n-1} \cdot \boldsymbol{\nabla}\mathbf{u}^n$, equations (2.5) become [39]

$$\mathbf{u}^n + \Delta t \mathbf{u}^{n-1} \cdot \boldsymbol{\nabla}\mathbf{u}^n - \Delta t \nu \boldsymbol{\nabla}^2 \mathbf{u}^n + \frac{\Delta t}{\rho} \boldsymbol{\nabla} P^n = \mathbf{u}^{n-1} \tag{2.9a}$$

$$\boldsymbol{\nabla} \cdot \mathbf{u}^n = 0, \tag{2.9b}$$

where $\Delta t = t^n - t^{n-1}$ is the time step. Equations (2.9) are still implicit in pressure, P^n, which (due to incompressibility) only occur in the momentum equation. The strategy of the IPCS is to replace this unknown pressure with P^{n-1}, and find the correct pressure and velocity fields in an algorithm that can be summarized as follows

1. Replace P^n with P^{n-1} and compute a tentative velocity $\mathbf{u}_*^n$ by solving (2.9a)
2. Find the pressure correction by requiring no divergence of a corrected tentative velocity (this gives a Poisson equation in pressure correction and $\mathbf{u}_*$)
3. Update pressure and velocity with the correction terms

The mathematical details of this algorithm is presented in chapter 4.1 in [39]. Formulating the resulting linear PDEs (equation (2.9a) in $\mathbf{u}_*$ and P^{n-1}, and a Poisson equation in pressure correction and $\mathbf{u}_*$) on weak form, the FEM can be applied to solve the problem. Expressing the field variables as linear combinations of the element shape (interpolation) functions, e.g. velocity as

$$\mathbf{u}_h = \sum_{i=1}^{N_{els}} \mathbf{U}_i \varphi_i, \tag{2.10}$$

a discretized version of the weak formulation is obtained [40]. In (2.10), $\mathbf{u}_h$ is the numerical approximation of the velocity $\mathbf{u}$, $\mathbf{U}_i$ are the unknown nodal degrees of freedom of element i, and φ_i are the known (chosen) element shape functions. N_{els} is the number of elements.

Since the weak form of the equations must be satisfied for an arbitrary choice of weighting functions $\mathbf{w}$, they can be chosen as $w_j = \varphi_j$. As a result, one will obtain a weak formulation in known shape functions and the unknown nodal degrees of freedom, which can be reduced to a system of algebraic equations [40]

$$\mathbf{AU} = \mathbf{L}, \tag{2.11}$$

where $A_{ij} = A(\varphi_i, \varphi_j)$ and $L_j = L(\varphi_j)$ are the weak form integral terms in the shape functions and known variables or constants (e.g. Δt, ν, u^{n-1} and P^{n-1} in the IPCS [39]). Finally, the system of (linear for IPCS) algebraic equations in equation (2.11) is to be solved or approximated with appropriate solver algorithms to determine the unknown nodal degrees of freedom $\mathbf{U}$.

Application of the CFD methodology requires either the use of specialized commercial or open source software, or programming of the solution algorithms. Irrespective of the choice, certain steps are involved when going from geometry to CFD-solution, summarized in table 2.2.1.

Step	Description
Meshing	The process of subdividing the computational domain into cells. Specialized software may be used, based on mathematical principles for generating meshes of high quality. Quality of the mesh is associated with the shape and regularity of the elements, such as low aspect ratios, blunt angles and low growth rate between adjacent cells.
Pre-processing	In the pre-processing step the fluid mechanical properties of the flow problem are defined. Material parameters for the fluid are assigned to the flow domain, such as viscosity and density. Further, the physics to be incorporated in the simulations are specified, e.g. turbulence modeling, unsteadiness or multiple phases. Finally, the boundary conditions are imposed on the outer bounds of the mesh.
Solving	Solving of the fluid flow problem is performed with solution algorithms that may be chosen by the analyst. The time steps and number of iterations (or convergence criteria) are specified, along with numerical parameters controlling the solution process, for instance relaxation terms and numerical diffusion coefficients.
Post-processing	The final step is post-processing of the obtained results. Field variables such as velocity and pressure are manipulated to express the desired results visually or numerically. Validation and verification of the results is also essential to assess the validity of the computed solution.

Table 2.2.1: CFD Methodology

Errors in CFD

It is important to stress that numerical solutions are only approximate, hence associated with errors. In CFD, errors can be categorized into:

- Modeling errors
- Discretization errors
- Convergence errors
- Round-off errors

The modeling errors are caused by discrepancies between the physical model and the actual physical system. These errors are strictly speaking not rising from the numerical approximation, but from the choice and simplification of PDEs and associated BCs. The significance of modeling errors can be evaluated through validation of the simulation results.

Discretization, or truncation errors are the errors associated with the discretization of the PDEs in time and space. They come from the difference between the exact solution of the PDEs and the solution of the numerical equations applied to represent the PDEs [41].

Convergence errors are due to the finiteness of iterations or mesh elements. The variation in the solution between consecutive iterations or different levels of mesh refinement is associated with how well the solution has converged. Iterative errors arise both in time (e.g. the number of time steps conducted until a convergence criteria or a periodic state is reached) and in the solution algorithms, where iterations may be required to solve a system of coupled (linear or non-linear) algebraic equations.

Round-off errors arise from the fact that only a certain number of digits (normally 32 or 64) can be stored for each floating point number in the calculations. A remedy is to set reference conditions equal to zero, provided that the absolute value of the variable is insignificant to the physics (for instance setting reference pressure to zero when simulating incompressible flows).

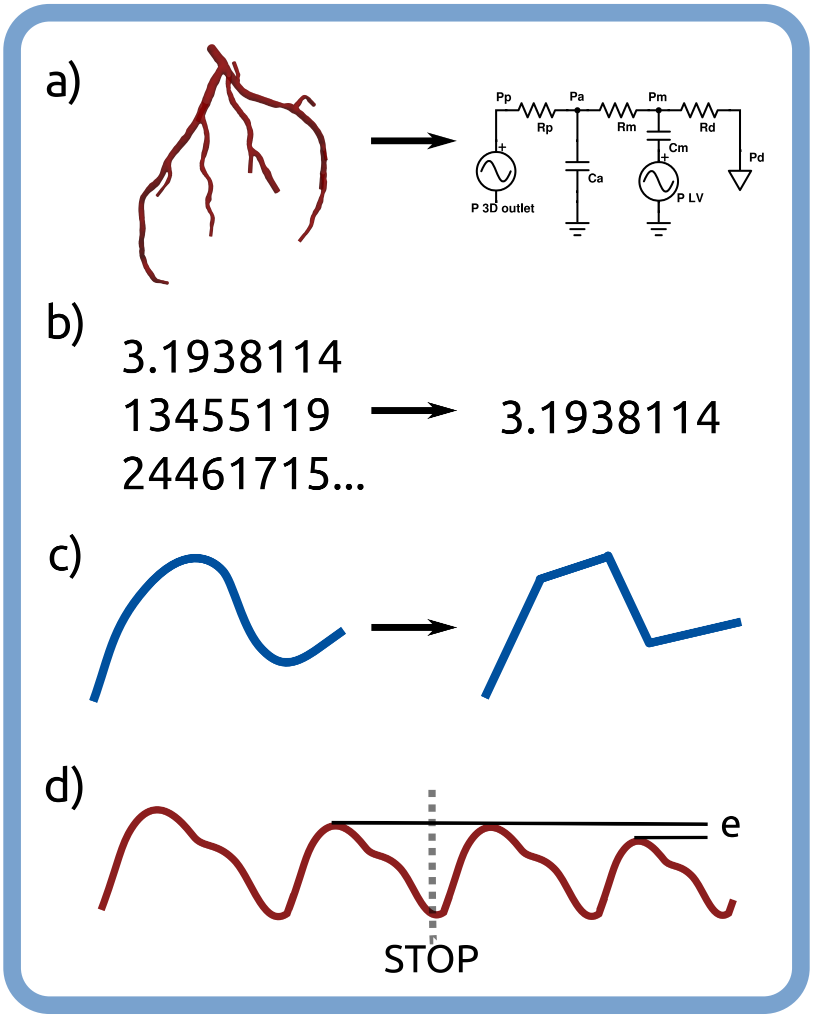

Figure 2.2.2: Types of errors in CFD: a) modeling errors, b) round-off errors, c) discretization errors and d) convergence errors.

The last three groups of errors are due to the finiteness of the FEM representation of infinite concepts. These errors can be assessed through verification analyses, evaluating the degree of improvement in the solution obtained from increasing the refinement levels, iterations or the order of the numerical methods applied.

Verification and validation play major roles in the assessment of CFD results. Validation of simulation results involves ensuring that the mathematical models represent the physical problem and characteristics sufficiently, whereas verification is the process of assuring that the mathematical equations are being solved correctly, through examining the errors caused by the discretization or implementation.

2.2.3 DIMENSIONLESS NUMBERS

Dimensionless numbers are applied in fluid mechanics to compare the relative contributions from different physical phenomena. The Reynolds[5] number is the ratio of inertial forces to viscous forces, and is defined as

$$Re_D = \frac{\rho u D}{\mu} \tag{2.12}$$

The denotation D signifies that the characteristic length dimension of the flow is a diameter, of for instance a tube or vessel. $\mu = \nu/\rho$ is the dynamic viscosity. Turbulence in flows are characterized by high Reynolds numbers, but is also dependent upon the geometry of the flow domain and the roughness of any confining walls [43]. Typical Re_D in the LAD is ∼400 [44], well below 2200, which is an approximate limit for transition to turbulence in hemodynamical flows[23]. However, stenoses and hyperemic conditions alter the local Reynolds number, and may provoke turbulence in the flow.

In periodic, pulsatile flows, it may be relevant to estimate the significance of oscillatory patterns in the flow. The Womersley[6] number is defined as

$$Wo = r_l \sqrt{\frac{\omega \rho}{\mu}}, \tag{2.13}$$

and represents a measure of the ratio of transient inertial forces to viscous forces, where ω is the angular frequency of the periodically pulsatile flow. For Wo larger than 3-4, unteadyness starts to become significant [23]. In flows where viscous forces are dominant (i.e. low Wo flows), velocity profiles exhibit small deviations from the parabolic profile given in equation (2.6), and can thus be regarded as quasi-steady [46]. Womersley numbers in the CAs are ∼2 under normal conditions [44].

---

[5] Osborne Reynolds (1842-1912), Irish physicist and innovator in fluid dynamics [42].

[6] John Ronald Womersley (1907-1958), British computer scientist and mathematician [45].

2.3 Coronary Flow Modeling

Combining the knowledge of coronary blood flow with fluid mechanics theory yields in the modeling principles for coronary flows. Many of these principles are common with general, arterial flow modeling. It is a common approach to describe arterial blood flow through an electrical analogy.

2.3.1 Electrical Analogy for Cardiovascular Flows

The main characteristics of hemodynamic flows can be adequately modeled by electrical circuits of resistors, capacitors and inductors in series and parallel. Relative pressure and volumetric flow rate are analogous to voltage and electric current in an electrical circuit respectively [22].

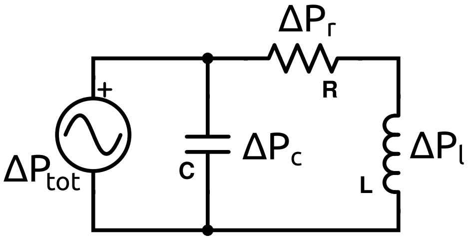

Figure 2.3.1: An electrical circuit as a model for arterial flow. ΔP_{tot} is the pressure potential, i.e.the total pressure drop over the modeled system. R, C, and L represents the resistance, compliance, and inductance of the system respectively.

The pressure potential is the pressure drop over a vessel length. The pressure required to sustain a given flow rate is affected by different physical phenomenons, such as wall friction, fluid inertia resisting acceleration, and elasticity of the vessel walls. The mechanical physics governing these resistances to flow has their electrical counterparts in resistance, inductance, and capacitance elements respectively [22]. The mechanical and analogous electrical equations are presented in table 2.3.1, originating from the physical laws denoted.

Mehcanical Equation	Electrical Equation
$\Delta P_r = RQ$ (2.14) *Poiseuille's equation*	$U = RI$ (2.15) *Ohm's law*
$\Delta P_l = L\frac{\partial Q}{\partial t}$ (2.16) *Newton's 2^{nd} law of motion*	$U = L\frac{\partial I}{\partial t}$ (2.17) *Inductance equation*
$\Delta P_c = \frac{1}{C}\int Q_c dt$ (2.18) *Material constitutive law*	$U = \frac{1}{C}\int I dt$ (2.19) *Capacitance equation*

Table 2.3.1: Mechanical and corresponding electrical equations. U is voltage, and I is the current.

ΔP_r, ΔP_l and ΔP_c are the viscous, inertal and capacitive pressure potentials respectively. Q_c is the flow into the capacitor, while R, L and C represents the viscous resistance, fluid inertance and wall compliance respectively. Assuming Poiseuille flow in an artery of constant, cylindrical cross-section, gives:

$$R = \frac{8\mu l}{\pi r^4}, \qquad L = \frac{\rho l}{\pi r^2}, \qquad C = \frac{3\pi r^3 l}{2Eh}, \tag{2.20}$$

where l is the vessel length. In the expression for C, E is the modulus of elasticity of the wall, and h is the wall thickness [47].

Equation (2.18) relates pressure potential over a capacitor with the flow rate into it. Since flow cannot run through the capacitor, the flow rate into it equals the rate of change of its volume. In the electrical terminology, the current into the capacitor equals the rate of change of its charge. Expressed mathematically, this becomes:

$$Q_c = \frac{\partial V_c}{\partial t}, \tag{2.21}$$

where V_c is the capacitive volume. Combining (2.21) with (2.18), gives the relation between the volume of the capacitor and the pressure potential required to sustain it:

$$\Delta P_c = \frac{1}{C} V_c \tag{2.22}$$

In a vessel, it is only physically meaningful to have capacitors in parallel with the running flow. The capacitor itself can be interpreted as a balloon being filled and emptied with blood.

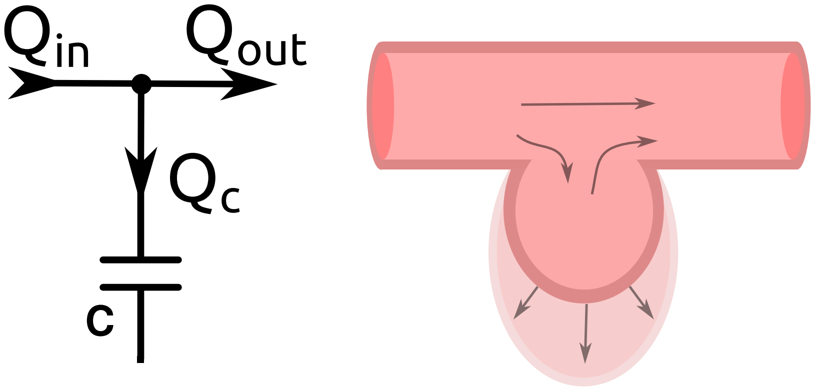

Figure 2.3.2: Mass conservation for a capacitor in parallel, $Q_{in} = Q_{out} + Q_c$, and an illustration of the balloon interpretation.

From conservation of mass, it is evident that the following holds for a capacitor in parallel:

$$Q_c = Q_{in} - Q_{out} \tag{2.23}$$

And further, combining equations (2.21) and (2.23),

$$\frac{\partial V_c}{\partial t} = Q_{in} - Q_{out} \tag{2.24}$$

2.3.2 Lumped Parameter Coronary Model

Lumped parameter models are 0D models incorporating the electrical elements presented above in circuits to model cardiovascular systems. The simplest type is the 2-element *Windkessel* model, with one resistance and one capacitance in parallel.

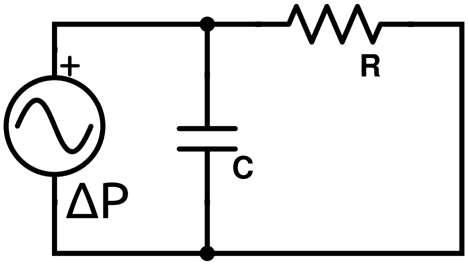

Figure 2.3.3: The 2-element Windkessel model of arterial flow. ΔP is total pressure drop (or potential) in the system, R is the resistance, and C is the compliance.

More comprehensive 3 and 4 element Windkessel models incorporate inductance as well. In the coronary arteries however, inductance (or inertance) can be neglected due to the relatively small diameters of the vessels [23, 48]. Another important feature determining coronary flow should however be emphasized: intramyocardial pressure, increasing the systolic resistance to flow. Mantero et al. [48] proposed a lumped parameter model incorporating the pressure from the left ventricle. A version of this model (hereafter referred to as cor-0D) is presented in the electrical circuit schematic in figure 2.3.4.

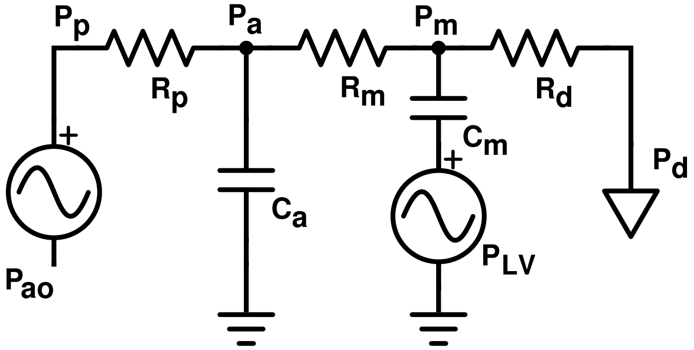

Figure 2.3.4: A lumped parameter model of the coronary circulation, modified from [48]. P aorta is the aortic pressure, equal to the pressure at the ostium of the coronary arteries. P_{LV} is the left ventricular pressure. P_p, P_a, P_m and P_d are the proximal (= P_{ao}, aortic pressure), arterial, intramyocardial and distal (venous) pressures respectively. R_p, R_m and R_d are the proximal, intramyocardial and distal resistances. C_a and C_m are the arterial and intramyocardial compliances.

The cor-0D model can also be represented by two coupled ordinary differential equations. Applying equations (2.22) with (2.24), the time derivatives of the pressure drops over the two capacitors in parallel are:

$$\frac{\partial(\Delta P_{ca})}{\partial t} = \frac{\partial P_a}{\partial t} = \frac{1}{C_a}(Q_p - Q_m) \tag{2.25a}$$

$$\frac{\partial(\Delta P_{cm})}{\partial t} = \frac{\partial(P_m - P_{LV})}{\partial t} = \frac{1}{C_m}(Q_m - Q_d) \tag{2.25b}$$

In equation (2.25), Q is denoted with the same index as the resistor it runs through (i.e. Q_m is the flow through R_m). Furthermore, the flow rates through the resistances are functions of resistances and pressures in the model according to (2.14).

2.3.3 BOUNDARY CONDITIONS

In any computational model of coronary circulation, the conditions on the boundaries of the computational domain has to be specified. 3D domains obtained from CT images are curtailed to the accessible image data of sufficient quality. Consequently, the domains are cut off when features are too small to be accurately captured by CT. When performing 3D CFD simulations, the pressure or velocity has to be prescribed at the inlet and outlets, as well as on the vessel walls. While inlet and wall conditions can be quite readily assumed (for rigid walls), conditions at the outlets are subject to great uncertainty, yet crucial for the final FFR results [49, 50]. 3D outlets are artificial boundaries in the sense that they usually do not constitute physically distinguishable locations in the CAs. As a result, outlets are commonly coupled with 1D or 0D models relating the outlet BCs to the conditions at locations that can be more precisely approximated [51].

WALLS

The no-slip condition requires velocity to be zero at the walls. Further, vessel walls may be modeled as either rigid or compliant. For the latter, a coupled structural and fluid mechanical problem has to be solved, which is associated with extensive computational effort. Hence, it is desirable to reduce the complexity by assuming rigid walls, provided that this does not affect the physiological resemblance of the model significantly.

INLET

At the inlet of a CA, conditions may be well estimated by clinical measurements. Aortic pressure waveforms can be obtained from measuring brachial blood pressure. Flow rates can also be assessed non-invasively, by novel ultrasound techniques: Transthoracic Doppler Echocardiography (TTDE) can be used to measure the flow rates in the main coronary branches [52]. Prescribing either a flow or a pressure waveform to the inlet are well established practices in unsteady hemodynamical CFD simulations [51].

OUTLETS

Imposing a pressure or flow rate to an outlet would constrain the interior solution to match a certain flow level or pressure drop in that branch. A more physiologically justified approach would be to let the flow distribute to the branches according to the resistance it meets in both the 3D domain, and at the boundaries (i.e. the peripheral resistances). By this approach, the total peripheral resistance is lumped at each outlet, coupling the outlet pressure and flow at each location by equation (2.14).

A further development of the lumped resistance outlet is a 2-element Windkessel model connected to the outlets. The compliance introduces the peripheral elasticity, incorporating the outlet flow's dependency on the rate of change of pressure. In coronary arteries, the peripheral resistances are highly dependent on the LV pressure [12]. Thus, a third option for setting the outlet conditions would be to use time varying resistances, or simply employ the cor-0D model to relate pressure and flow. Still, the total peripheral resistances of the coronary sub-trees downstream the 3D outlets have to be determined. This can be done by using Murray's law.

Murray's Law

Murray's law is based on the principle of evolutionary optimization of shapes to minimize energy requirements in biological systems. It states that vessel radius is a function of the flow it conveys, governed by the minimization of hemodynamic power requirements. Published by Murray in 1926 [53], the law relates the radius to flow in a vessel as:

$$Q_i = kr_i^3 \tag{2.26}$$

Equation (2.26) assumes Poiseuille flow, i.e. that the viscous forces are proportional to r^{-4}, and further that the metabolic power is proportional to the vessel volume, or r^2. Combining equation (2.14) and (2.26), the peripheral resistance of a branch, R_i is related to the radius as

$$R_i \propto r_i^{-3} \tag{2.27}$$

Murray's law is widely applied in distributing peripheral resistances for coronary flow modeling [13, 54, 55]. However, it has its limitations, as it is based on strict assumptions of the geometrical configuration of arterial trees. Other methods for determining terminal resistances have been proposed, relying more on empirical observations [56–58].

3

Methods

This chapter is concerned with the methodology developed and applied in CFD simulations of coronary flows for $\mathrm{FFR}_{\mathrm{CT}}$ computations in the LCA. The first section presents the computational models employed in the simulations. Section 3.2 relates the models to patient data, and how these are used in patient-specific simulations. A considerate part of the work has consisted in developing physiologically and computationally valid models and methods. More than 200 cardiac cycles have been simulated until reaching the final setup. The methodology was developed incrementally, continuously performing validation and verification work. The verification and validation methods used are presented in sections 3.3 and 3.4, respectively. Finally, section 3.5 describes the statistical treatment of transient and steady simulation results.

3.1 COMPUTATIONAL MODELS

The computational model applied in CFD simulations consists of a 3D domain of the LCA, where the 3D incompressible N-S equations are solved, coupled with the lumped parameter model cor-0D connected to the outlets. Input to the model is the inlet pressure waveform, the left ventricle (LV) pressure and patient-specific model parameters. The model is illustrated in figure 3.1.1.

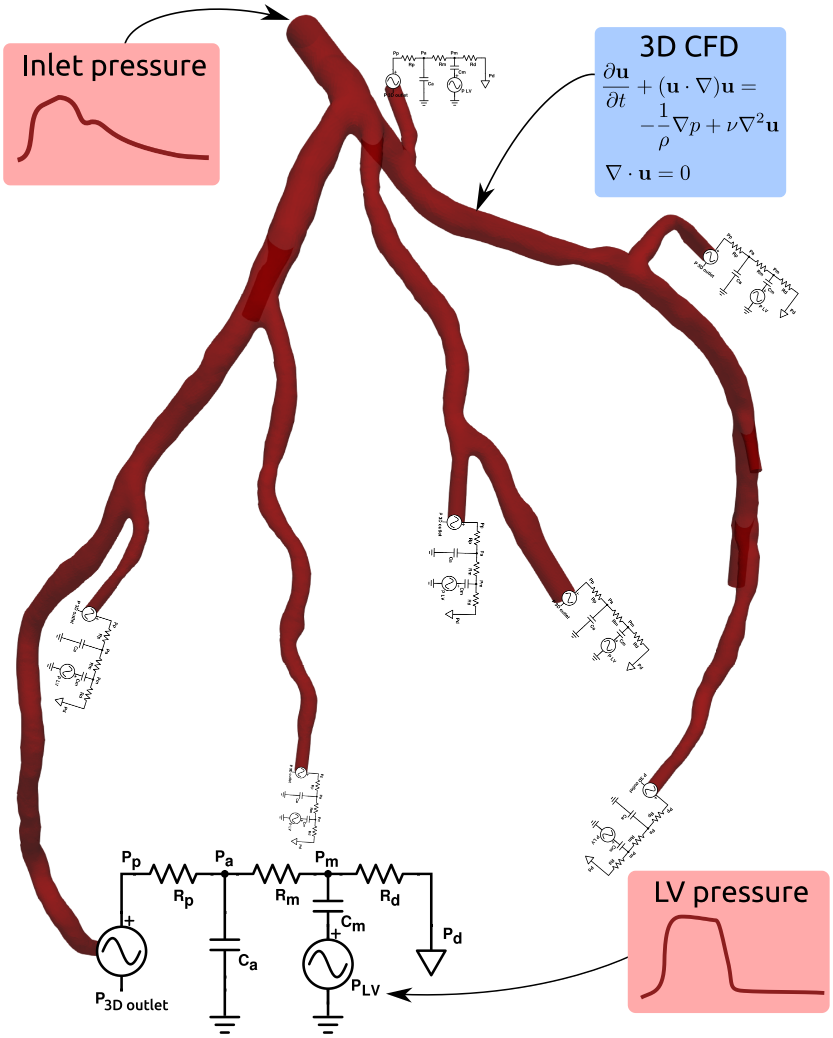

Figure 3.1.1: Computational model of coronary artery flows. Details of the lumped parameter outlet model are presented in 2.3.2.

All software used in the present work are either licensed with open source, or developed in-house. Table 3.1.1 gives a presentation of the software and utilities applied.

Software	Description
Python [59]	An open source programming language affiliated with a plethora of packages, continuously updated by contributors from all over the world.
VMTK [60]	The Vascular Modeling Toolkit (VMTK) is an open source project consisting of a framework for the segmentation and meshing of 3D geometries from CT images.
FEniCS [61]	A collection of software components forming a general purpose FE solver for differential equations. It is developed by the FEniCS Project, which is licensed under the GNU General Public License (GPL) as free software.
cbcflow [62]	An assembly of solvers for solving fluid mechanical problems governed by the incompressible N-S equations. It builds on the FEniCS library, and is licensed under the GNU GPL.
coronary3D	A python implementation of the computational model in figure 3.1.1, and configuration script for cbcflow, defining a coronary flow problem. Developed in-house in the Biomechanics Division at the Department of Structural Engineering, NTNU, with the present work contributing with implementations and development.
coronary0D	A python implementation of the cor-0D model, solved for a given inlet pressure or flow waveform, LV-pressure waveform and constant venous pressure. The source code is found in appendix B.
ParaView [63]	An open source post-processing tool for visualization and analysis of large datasets.

Table 3.1.1: Computational software and utilities used in this thesis.

Python, with related packages, was used for everything from plotting of results to implementation of the computational models. VMTK was employed in the segmentation and meshing process. The flow in the 3D domain was solved by using FEniCS, through the *cbcflow* module. Defining the patient-specific flow problems and computation of the cor-0D BCs was performed in the *coronary3D* python script, and the *coronary0D* script was an aid for validation and rapid prototyping of model parameters. ParaView was used in the post-processing of the CFD results. A comprehensive description of the computational models developed and applied follows.

3.1.1 Numerical Methods

3D CFD

The problem to be solved is governed by the unsteady, incompressible N-S equations in 3D, with Dirichlet BCs (pressure specified at the 3D inlet and outlets). Linear Lagrange P_1 tetrahedral elements (figure 2.2.1) were applied for interpolation of the field variables in pressure and velocity. The time step Δt was 0.001 s in the transient simulations, except cases where a Δt of 0.0005 s was necessary to avoid diverging solutions. Transient simulations were run for 5 or 10 cycles with period of 0.8 s. In the stationary case, Δt was 0.0001 s, and simulations were run for 1000 iterations. The only other difference between the steady and unsteady simulations was in the boundary conditions. Floating point numbers were stored with 64 digits.

The FEniCS extension *cbcflow* [62] was used for the computations presented in this work. This tool provides efficient implementations of schemes to solve the incompressible N-S equations, as well as a framework for implementation of lumped parameter models and assignment of BCs. The incremental pressure correction scheme (IPCS) implemented in *cbcflow* was used for the coupling of pressure and velocity fields. This scheme is based on a multistep technique proposed by Goda [64], and involves the calculation of a tentative velocity field each time step based on the previous pressure solution. The N-S equations are linearized to first order accuracy, semi-implicit in the convection term (see equation (2.9) and [39] for more details).

Numerical diffusion was enabled through specifying a streamline diffusion coefficient (*sdc*) in the solution algorithm of *cbcflow*. Numerical streamline diffusion introduce an artificial diffusion term to the N-S equation acting only in the advection direction of the flow [61]. The use of numerical diffusion was motivated by stability issues experienced in the development of the computational methodology. Higher values of *sdc* ($\in [0,1]$) means stronger weight to the numerical diffusion term.

3D/0D Coupling

The coupling of 3D outlet boundaries with the cor-0D model was implemented in *coronary3D*. During the transient simulations, the outlet BCs for the subsequent time step are updated from the results of the cor-0D model. The pressure at the next time step was set to a computed proximal pressure in the 0D model, P_p. The exact value of P_p^{n+1} comes from equation (2.14) applied on the resistor R_p in cor-0D:

$$P_p^{n+1} = P_a^{n+1} + R_p Q_p^{n+1} \tag{3.1}$$

Q_p^{n+1} in (3.1) should equal the 3D outlet flow on the next time step, Q_{3D}^{n+1}. Since this is not known *a priori*, but is a result of the 3D CFD solution at the next time step (with a given BC of P_{3D}^{n+1}), the above formulation is implicit in time. To solve this condition exactly would require iterations on the subsequent time step to ensure matching flow in the cor-0D model and out of the 3D domain. In the present simulations however, Q_p^{n+1} was approximated by Q_{3D}^n. Thus, the outlet BC for the subsequent time step was set as:

$$P_{3D}^{n+1} := P_a^{n+1} + R_p Q_{3D}^n \tag{3.2}$$

P_a^{n+1} was computed by the explicit Euler method applied to equation (2.25a) in chapter 2, giving

$$\frac{P_a^{n+1} - P_a^n}{\Delta t} = \frac{1}{C_a}(Q_p^n - Q_m^n) = \frac{1}{C}\left(Q_{3D}^n - \frac{P_a^n - P_m^n}{R_m}\right) \tag{3.3}$$

Similarly, the other pressures in the 0D model were updated with the explicit Euler method on (2.25b).

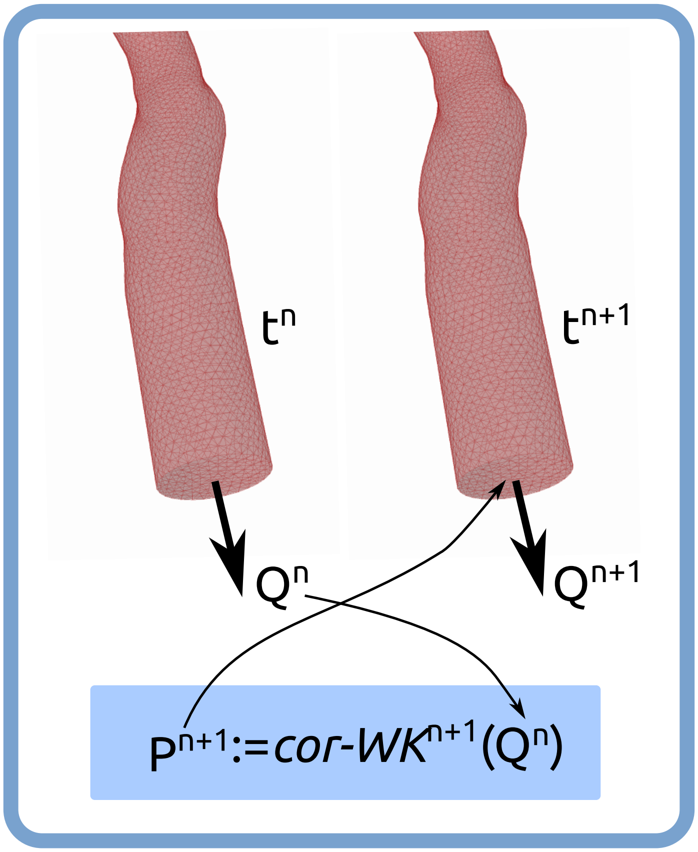

Figure 3.1.2: Coupling of the 3D and cor-0D model at the outlets. P_p from the cor-0D solution at next time step, assuming $Q_p^{n+1} = Q_{3D}^n$, is imposed on the boundary.

3.1.2 Boundary conditions

Boundary conditions were assigned to the walls, inlet and outlets of the 3D domain. The vessel walls were modeled as rigid, and assigned with the no-slip BC for velocity in all simulations.

Transient Boundary Conditions

A generic aortic pressure waveform was assigned to the inlet, adapted from Kim et al. [65], and adjusted to patient measurements of mean and pulse pressure. At the outlets, the lumped parameter model cor-0D was assigned, as a model of the coronary sub-tree distal to the outlet. Thus, the proximal pressure in the model, P_p represents the pressure at the 3D outlet (rather than the aortic pressure, as in figure 2.3.4). The incentive for using this model was to obtain physiological shapes and phase shifts of the pressure and flow waveforms. The distal pressure in the model, P_d, was assumed to be constant, and equal to a venous pressure of 5 $mmHg$. The left ventricle pressure was specified through a waveform obtained from Kim et al. [65] (to ensure it was in phase with the inlet aortic pressure curve). The applied pressure waveforms are shown in figure 3.1.3.

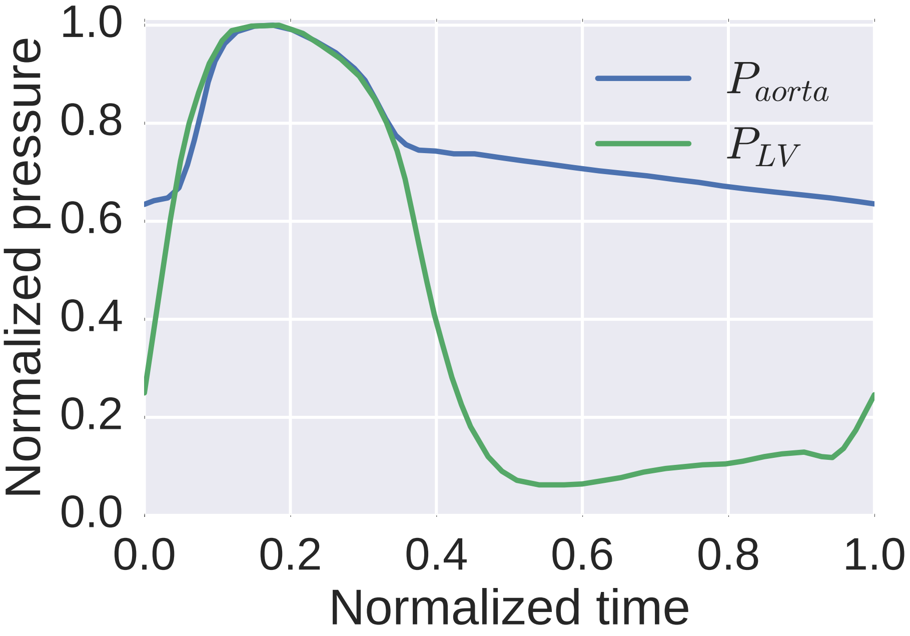

Figure 3.1.3: Input waveforms of normalized aortic and LV pressure. Used as input to the computational model, and tailored to patient-specific pressures.

The total peripheral resistance R_{tot} and total compliance C_{tot} of the coronary tree were specified in the input parameters. R_{tot} was corrected each cardiac cycle to match a given hyperemic target flow rate in the LM artery. This was performed by computing the difference between the average inlet flow the previous cycle and the target flow rate, and then compute R_{tot} for the next cycle as

$$R_{tot}^{c+1} = (1 - \gamma \cdot \delta Q) \cdot R_{tot}^{c}, \tag{3.4}$$

where c is the number of the cycle, γ is a relaxation coefficient (=0.9) and $\delta Q = Q_{target} - \bar{Q}_{inlet}$.

R_{tot} and C_{tot} were further distributed to the outlets. The inverse of R_{tot} equals the sum of the inverse of n_o parallel outlet resistances:

$$\frac{1}{R_{tot}} = \sum_{i=1}^{n_o} \frac{1}{R_i} \tag{3.5}$$

Resistances were assumed to be proportional to the inverse of the terminal vessel radii cubed, according to Murray's law (2.27), and distributed between the outlets of the flow domain accordingly. Combining equations (2.27) and (3.5) gives:

$$R_i = \frac{\sum_{j=1}^{n_o} {r_j}^3}{{r_i}^3} R_{tot} \tag{3.6}$$

The total equivalent capacitance is the sum of all parallel outlet capacitances [23]. From equation (2.20), arterial compliance scales with r^3. Accordingly, C_{tot} was distributed between the outlets as follows:

$$C_i = \frac{{r_i}^3}{\sum_{j=1}^{n_o} {r_j}^3} C_{tot} \tag{3.7}$$

Furthermore, the resistance and compliance of each outlet, R_i and C_i was distributed between the parameters in the cor-0D model. The fractions of R_i in R_p, R_m and R_d were set to 0.35, 0.5 and 0.15 respectively. Similarly, C_i fractions were 0.1 and 0.9 in C_a and C_m. These values were chosen to obtain physiological flow waveforms, ensured by the validation work outlined in 3.4. Previous work using the cor-0D as outlet BCs in coronary CFD simulations was consulted in the process [65].

At every time-step, the pressure P_p computed from the cor-0D model was assigned to each 3D outlet, as explained in 3.1.1.

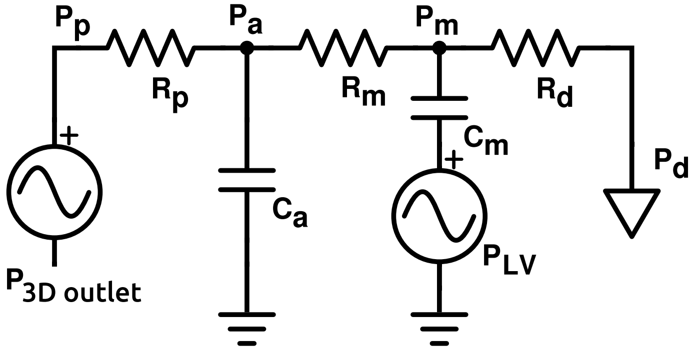

Figure 3.1.4: The cor-0D model as applied on the outlet boundaries of the 3D domain. Parameters are explained in figure 2.3.4.

STEADY BOUNDARY CONDITIONS

For the steady simulations, the main objective when specifying the BCs was to ensure consistency with the transient simulations. For comparison of steady and transient FFR_{CT} computations, the steady BCs should equal the time averaged transient BCs. At the inlet, a constant pressure equal to the average transient inlet pressure was assigned. Each outlet was given a resistance equal to the average, equivalent resistance of the cor-0D model, computed as:

$$R_{eq,i} = \frac{\bar{P}_{p,i} - P_d}{\bar{Q}_i} \tag{3.8}$$

Consequently, neither pressure nor flow is constrained to specific values at the outlet, only the relation between them. As a result, the magnitudes of flow and pressure at the outlets are solutions of the interior 3D calculations, where any discrepancy from the average transient solution is due to the loss of unsteady flow patterns. As opposed to the unsteady BCs, the total resistance was not updated to match the target flow in the steady simulations, to ensure comparability between the steady and transient results.

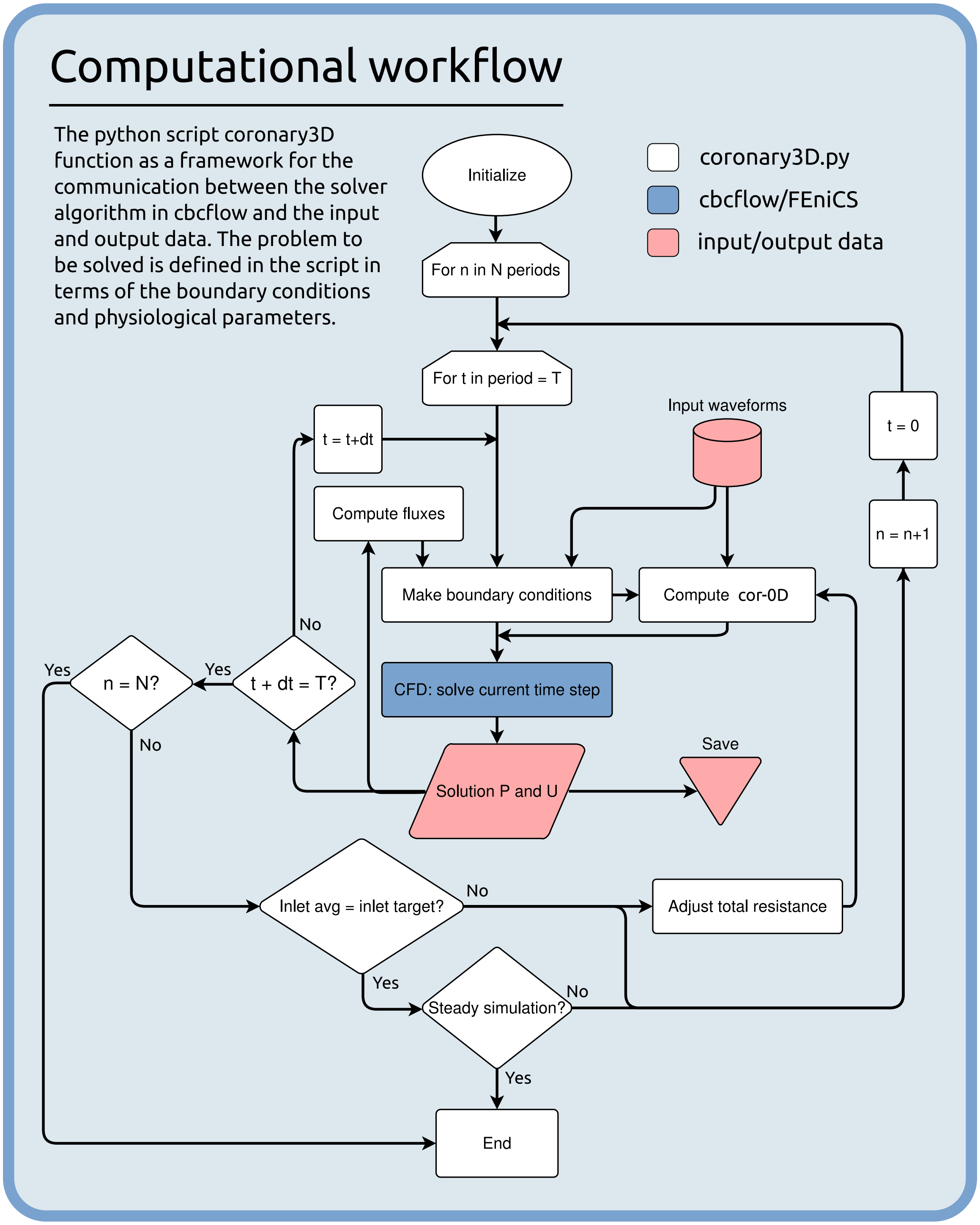

Computational workflow

The python script coronary3D function as a framework for the communication between the solver algorithm in cbcflow and the input and output data. The problem to be solved is defined in the script in terms of the boundary conditions and physiological parameters.

Figure 3.1.5: Schematic overview of the computational workflow.

3.2 PATIENT-SPECIFIC MODEL SETUP

Clinical measurements and CT images from patients recruited for the pilot study of NTNU's $\mathrm{FFR}_{\mathrm{CT}}$ research project were used to make patient-specific models.

3.2.1 SEGMENTATION AND MESHING

CT (CCTA) images of the patients were used with VMTK to create the 3D flow domains and the computational grids. The pipeline for generating meshes was:

1. Read and enhance CCTA image file set
2. Create level set for segmentation
3. Make geometry of level set and prepare for meshing
4. Generate computational mesh

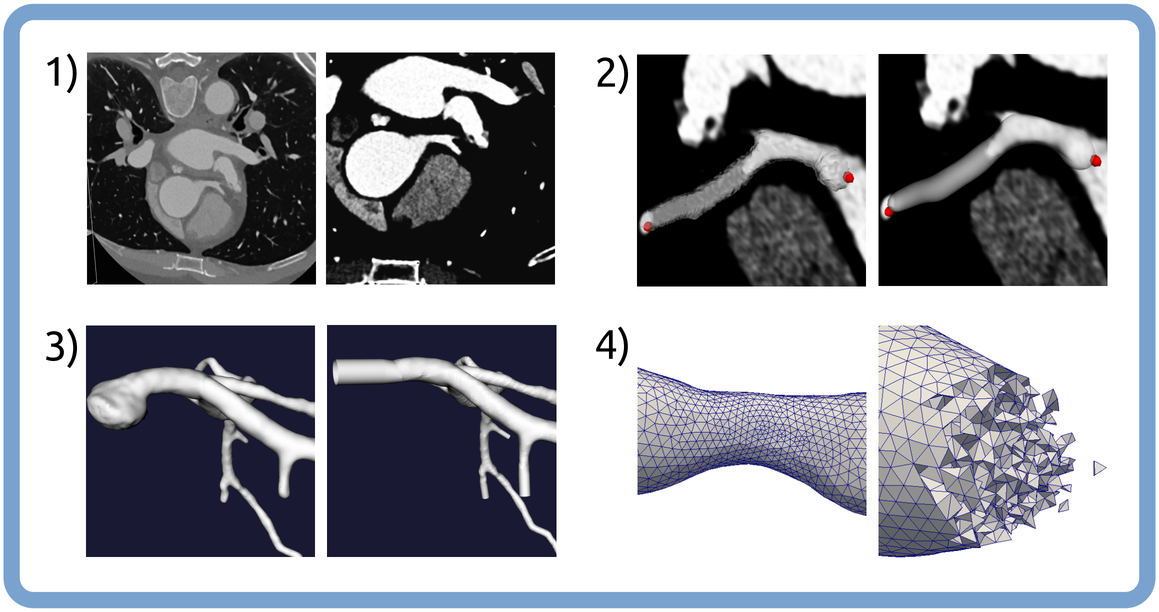

Figure 3.2.1: The four steps involved in making a patient-specific computational mesh. 1) original and enhanced CT image, 2) initial and modified level set of a CA segment, 3) geometry before and after clipping and adding extensions to inlet/outlets and 4) radius adapted mesh of tetrahedral cells.

- In step 1, the image files were processed. To facilitate the segmentation process, the contrast and exposure was altered by using the *scikit-image*[1] python algorithm *exposure* with intensity levels of tissue and plaque as input parameters.

- Step 2 involved setting the intensity levels for each partition of the CAs to be modeled. In VMTK, this was performed using the *colliding fronts* method. Parameters controlling the inflation, regularization and attraction to the image gradients at the lumen surface were specified for each segment. This process relies heavily on the operator's interpretation of the images.

- The complete segmented geometry was created in step 3, based on the levels set in step 2. To prepare the geometry for CFD meshing, outlets and inlets were cut to obtain plane, normal faces for the boundaries. Furthermore, normal extensions of the inlet and outlets were created using the VMTK routine *vmtkflowextensions*. Extensions of a length 4 times the radius of the inlet/outlets were assumed to be sufficient to elude artificial constraints on the flow domain of interest. In cases where it was found necessary, the *vmtksurfacesmoothing* was applied to filter out non-physiological unevenness.

- In the final step, the computational mesh was generated. VMTK offers the opportunity to create radius adapted mesh, which was employed in the present work. Radii are computed from the maximal inscribed sphere at each point along the centerlines of the flow domain. This data is used to set the element size according to the radius at each point, ensuring a relative measure for the refinement of the mesh throughout the domain. Specifying the *edgelengthfactor* in VMTK controlled the refinement of the meshes. All meshes were built up of tetrahedral cells.

3.2.2 Physiological Parameters and Boundary Conditions

For every patient, the clinical measurements were employed to set the BCs and to estimate the hyperemic flow conditions.

The pressure curve assigned to the inlet was scaled to match the MAP for each patient, as well as the pulse pressure (PP), computed as PP = SBP - DBP. The LV pressure curve was adjusted to

---

[1] scikit-image: a collection of image manipulation Python modules developed in the SciPy community [66].

match a maximal pressure equal to the SBP. The total flow rate in the LM was approximated to be 2% of the CO for all patients. This was based on the assumption that 50% of the coronary flow would be conveyed through the left coronary tree, and that total coronary flow is approximately 4% of the CO [11].

As the clinical measurements provided were baseline data, assumptions were made on the hyperemic flow conditions. First of all, it was assumed that the pressures remained unaltered in the hyperemic state. The target hyperemic flow rate, Q_{target}, was assumed to be four times the estimated baseline coronary flow. This is a pragmatic average of results from studies on adenosine induced hyperemia [27–29].

Based on the target hyperemic flow, the initial guess of the total coronary resistance R_{tot} was computed as

$$R_{tot}^{1} \approx \frac{\Delta P}{Q_{target}} = \frac{MAP - P_d}{Q_{hyp}} \tag{3.9}$$

This value was updated each cycle to match the target flow rate by equation (3.4). For the steady simulations, the resistance at each outlet was computed as shown in equation (3.8), and kept constant.

Some parameters were *not* set specific for each patient. These includes the rheological properties of blood, modeled as a Newtonian fluid with a density of $\rho = 1.50\ g/cm^3$ and a constant dynamic viscosity of $\mu = 0.035\ g/(cm\cdot s)$. In addition, venous (distal) pressure, $P_d = 5\ mmHg$, the total coronary compliance $C_{tot} = 0.056\ cm^3/mmHg$, and the period $T = 0.8\ s$ were set equal in all patients.

3.3 VERIFICATION

In this thesis, verification was performed by ensuring mesh independent results, periodic and iterative convergence in the variables of interest for this thesis, pressure and FFR, and evaluating the effect of numerical diffusion. Verification of the implementation of solvers in *cbcflow* and comparison with analytical solutions has already been performed by Valen-Senstad et al. [38]. All verification results are presented in the next chapter, section 4.2.

Comparison of meshes was conducted on three patient geometries. Four meshes of different refinement were made from each geometry, consisting of approximately 0.5 million (M), 1M, 2M and 3M elements. The refinement level was controlled by adjusting the *edgelengthfactor* (*elf*) in VMTK. An initial guess of the *elf* would give a mesh of N_{els} elements. A desired mesh size of $f \cdot N_{els}$ elements was then obtained by multiplying the initial *elf* by a factor of $\sim \sqrt[3]{f}$. Transient simulations were run for 10 or 5 cardiac cycles. For two of the patients the total resistance R_{tot} was updated each cycle to match a target flow rate. On the last patient, R_{tot} was kept constant. Otherwise, simulation methodology was as explained in sections 3.1 and 3.2.

Errors in pressure and FFR were analyzed by comparing with the 3M solutions. The error in pressure at a location i of a k million mesh was computed as

$$e^m_{P,i} = \frac{\bar{P}^{3M}_i - \bar{P}^{kM}_i}{\Delta P^{3M}_{avg}}, \tag{3.10}$$

where $\bar{P}_i$ is the average pressure of the last cycle, and ΔP^{3M}_{avg} is the average pressure drop between inlet and outlets in the model.

The error in FFR was evaluated in the absolute difference, as FFR is already normalized to the inlet pressure:

$$e^m_{FFR,i} = FFR^{3M}_i - FFR^{kM}_i \tag{3.11}$$

FFR for a location i was computed as

$$FFR_i = \frac{\bar{P}_i}{\bar{P}_{inlet}}, \tag{3.12}$$

Results from a selection of interior locations and all outlets were analyzed. The method for selecting locations and computing pressure is described in section 3.5.

Convergence to a periodic state was ensured by monitoring the residual in mean cyclic pressure at the 3D outlets throughout the simulations. In addition, two simulations were run on different geometries for 10 cycles to determine the required number of cycles to reach convergence. The residuals δ^c in pressure and FFR for a cycle c was assessed for all outlets according to equations

(3.13) and (3.14), where *i* indicates an outlet.

$$\delta^c_{P,i} = \frac{\bar{P}^c_i - \bar{P}^{c-1}_i}{\Delta P^c_{avg}}, \tag{3.13}$$

$$\delta^c_{FFR,i} = FFR^c_i - FFR^{c-1}_i \tag{3.14}$$

Similarly, residuals δ^i were computed for every iteration for steady simulations.

Finally, an observation was made on the significance of the streamline diffusion coefficient *sdc* in the numerical solution algorithm. Three transient simulations were run on the same mesh, with *sdc* of 0.25, 0.5 and 1.0 respectively. The error relative to the *sdc* = 0.25 results was computed for pressure and FFR in the same manner as in equations (3.10) and (3.11).

3.4 VALIDATION

Validation of the computational model presented so far involved comparison with related work. In addition, comparison was made with results from the lumped parameter model cor-0D, as a model for the complete LCA circulation. Emphasis was put on the comparison of flow waveforms, not being constrained in the model (but computed as a result of the interaction between the 3D and 0D models).

The process of tuning the cor-0D model parameters to obtain physiological relationships between pressure and flow required running several 3D CFD simulations. This process was time consuming, as the simulation of at least one cardiac cycle at fairly large meshes was necessary to obtain any valuable information. However, early simulation results indicated that the pressure and flow waveforms experienced marginal changes in shape throughout the 3D domain. This motivated employing the cor-0D model as a simplified model for the complete LCA circulation to rapidly assess the effect of changing the model parameters. The cor-0D model was implemented in a separate python script, *coronary0D*, and solved with explicit Euler method in time. With an inlet waveform prescribed to the proximal pressure P_p, a resulting flow curve for a given configuration of the model parameters was obtained within seconds.

Transient and steady $\mathrm{FFR}_{\mathrm{CT}}$ results were compared with available data from clinically measured FFR. These results were not emphasized in the validation of the computational model as a tool for comparison of steady and transient simulations. Replication of clinical measurements is still too ambitious with the present model and methodology, until they are further developed.

Finally, a qualitative evaluation of the flow in critical regions of the 3D domains was performed. The simulation results were analyzed in stenotic regions of some of the patient geometries with prominent stenoses. Local Reynolds and Womersley numbers were computed, and flow patterns were inspected through velocity profiles and streamlines.

3.5 STATISTICAL ANALYSIS

Statistical analysis was performed to compare transient and steady simulation results. The mean pressures were computed at selected locations in the 3D domain and at all outlets. Interior locations were chosen from relevance to FFR, i.e. distal to stenoses (where prominent) or distal in the main branches of the CAs. Pressures were computed from the spatial averages on cross-sections normal to the flow direction using ParaView. Furthermore, all time averages were computed over the last cardiac cycle simulated.

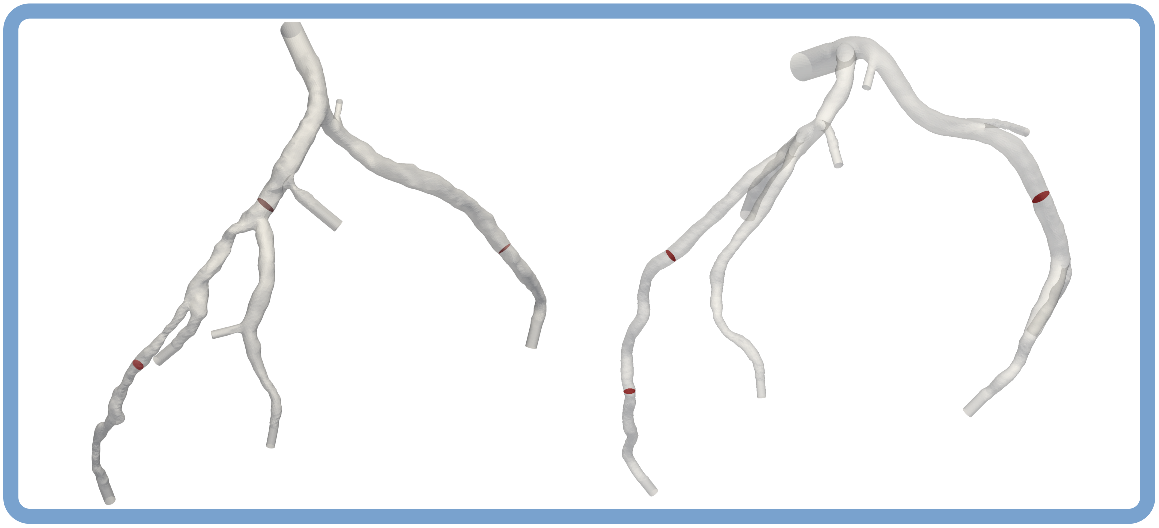

Figure 3.5.1: Examples of interior locations used to compare steady and transient CFD results.

Differences in pressure and FFR were computed for each location. The errors of the steady solution at a location i were computed by equations (3.15).

$$e^s_{P,i} = \frac{\bar{P}^t_i - \bar{P}^s_i}{\Delta P^t_{avg}} \tag{3.15a}$$

$$e^s_{FFR,i} = FFR^t_i - FFR^s_i \tag{3.15b}$$

FFR_i is defined as stated in equation (3.12), and ΔP^t_{avg} is the average pressure drop from inlet to outlets of the transient solution. X^t and X^s are transient and steady results respectively. Errors were assessed both on a per patient level, and a per location level. Mean absolute error (MAE) for a patient was computed as $mean(|e^s_{P/FFR}|)$ over the error sampling locations in that patient's LCA. In addition, the root mean square error (RMSE) metric was computed for the errors in (3.15) as

$$RMSE_{FFR/P} = \sqrt{\frac{1}{n_{loc}} \sum_{i=1}^{n_{loc}} (e^s_{FFR/P,i})^2}, \tag{3.16}$$

where n_{loc} is the number of locations. Since RMSE sums squares of errors, larger errors are penalized more than what is the case with MAE.

Per location, the correlation between FFR and errors were evaluated, as well as the maximal errors of each patient. In addition, correlation between errors and local Womersley numbers was assessed.

Errors were analyzed with statistical tests. Normality of the error distributions was tested with the *Shapiro-Wilk* test for small sample data. The null hypothesis is normally distributed data, with low scores ($W \in [0,1]$) indicating skewness or kurtosis in the distribution [67]. Difference between errors at interior locations and outlets was further evaluated with the the *Mann-Whitney U* test, with the null hypothesis that errors from one sample is just as likely to be larger as smaller than the mean of the other sample. Correlations were assessed with the non-parametric Spearman's rank order correlation coefficient (*Spearman's rho*) and linear regression. All statistical analyses were performed with the *stats* module in the Python package *SciPy* [68].

Finally, the average percentage errors in outlet flows were computed for each patient as

$$e_Q^s = \frac{1}{n_o} \sum_{i=1}^{n_o} \frac{Q_i^t - Q_i^s}{Q_i^t} \cdot 100, \tag{3.17}$$

where Q_i^t and Q_i^s are the flows out of outlet i for transient and steady simulations.

4

Results

This chapter contains the presentable results from this project's work. Section 4.1 is concerned with the results from patient-specific modeling, i.e. LCA geometries and mesh, and personalized simulation parameters. Sections 4.2 and 4.3 treats the results from verification and validation of the simulation methodology and results. Finally, in section 4.4, steady and transient simulation results are compared and analyzed.

All modeling and simulation was performed using two different workstations with specifications: (i) 15 x Intel Xenon Processor E5-2630 v4 3.1GHz (10 cores), 32GB (8x4GB) RAM, and (ii) 8 x Intel Core i7-4790 CPU (4 cores) 3.60GHz, 32GB (8x4GB) RAM.

4.1 Patient-specific Models

8 of the patients recruited at St. Olavs Hospital, Trondheim for the pilot study of NTNU's FFR_{CT}-project were incorporated in the work. In the following, patients are denoted by their pilot ID for consistency with the research project. Pilot 8 was excluded due to bad CT image quality. The clinical measurements from St. Olavs Hospital were reported as presented in table 4.1.1. CO is based on velocity measurements by PW Doppler[1] ultrasound, and MAP has been computed from SBP and DBP according to

$$MAP = \frac{1}{3}SBP + \frac{2}{3}DBP \tag{4.1}$$

Pilot ID	Sex	HR $[bpm]$	MAP $[mmHg]$	SBP $[mmHg]$	DBP $[mmHg]$	CO $[l/min]$
1	F	66	95.6	119	84	3.8
2	F	57	83.6	123	64	4.1
3	M	73	92.6	122	78	6.2
4	M	67	105.6	139	89	5.5
5	M	62	88.3	115	75	6.8
6	M	50	97.7	133	80	6.5
7	M	54	99.6	151	74	5.5
9	M	52	84	116	68	5.3
Mean		60.13	93.38	127.25	76.50	5.46
±SD		±8.17	±7.76	1±2.68	±8.14	±1.07

Table 4.1.1: Clinically measured baseline data of the patients. The pilot ID refers to the identifications used in the related research project, HR (heart rate), MAP (mean arterial pressure), SBP (systolic blood pressure), DBP (diastolic blood pressure) and CO (cardiac output) and SD = standard deviation.

3D geometries and computational meshes were generated following the steps in 3.2.1. The resulting meshes applied in steady and transient simulations are listed in table 4.1.2.

---

[1] Pulsed-Wave Doppler: pulsed signal ultrasound for localized measurements of blood flow velocity [69].

Pilot ID	n_o	N_{els}
1	5	1241329
2	5	914716
3	8	940891
4	7	1378784
5	11	1230978
6	8	1150302
7	11	963708
9	6	1288344

Table 4.1.2: Computational meshes for transient and steady simulations. n_o is the number of outlets, and N_{els} is the number of tetrahedral elements in the mesh.

The patient-specific parameters employed in the simulations were computed and used as described in 3.2.2, and are summarized in table 4.1.3.

Pilot ID	MAP $[mmHg]$	$P_{LV,max}$ $[mmHg]$	PP $[mmHg]$	Q_{target} $[ml/s]$	R^1_{tot} $[mmHg \cdot s/cm^3]$
1	95.6	119.0	35.0	5.07	17.88
2	83.6	123.0	59.0	5.47	14.38
3	92.6	122.0	44.0	8.27	10.60
4	105.6	139.0	50.0	7.33	13.72
5	88.3	115.0	40.0	9.07	9.19
6	97.7	133.0	53.0	8.67	10.70
7	99.6	151.0	77.0	7.33	12.90
9	84.0	116.0	48.0	7.07	11.18
Mean ±SD	93.38 ±7.76	127.25 ±12.68	50.75 ±12.98	7.28 ±1.43	12.57 ±2.77

Table 4.1.3: Patient-specific simulation parameters. Pressures were used to scale the input waveforms. Q_{target} is the hyperemic target flow in the LM, and R^1_{tot} the initial (first cycle) total resistance.

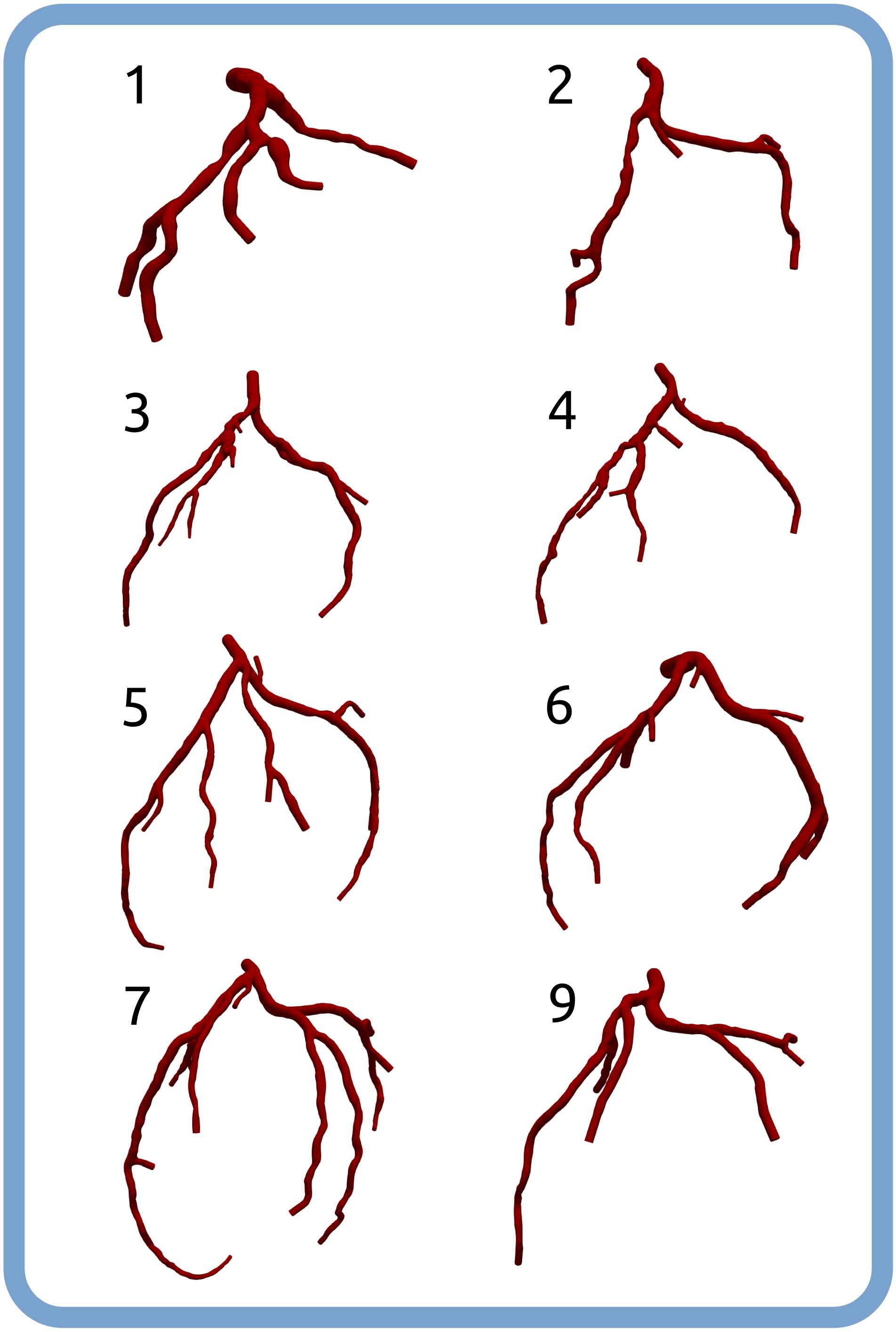

Figure 4.1.1: All patient 3D models of the LCA (numbered by pilot ID).

4.2 VERIFICATION

Coupled 3D-0D CFD simulations of hyperemic coronary blood flows were performed with models and methods as presented in the previous chapter. The details of the verification methods was described in 3.3.

4.2.1 MESH STUDY

The meshes used to compare refinement levels are listed in table 4.2.1. Examples of the different meshes are presented in figure 4.2.1.

Pilot ID	No. of elements			
	0.5M	1M	2M	3M
2	531973	914716	2078932	3090150
5	782444	1230978	2105123	3071280
7	651131	963708	1952472	2915975

Table 4.2.1: Meshes for mesh study of approximately 0.5M, 1M, 2M an 3M elements.

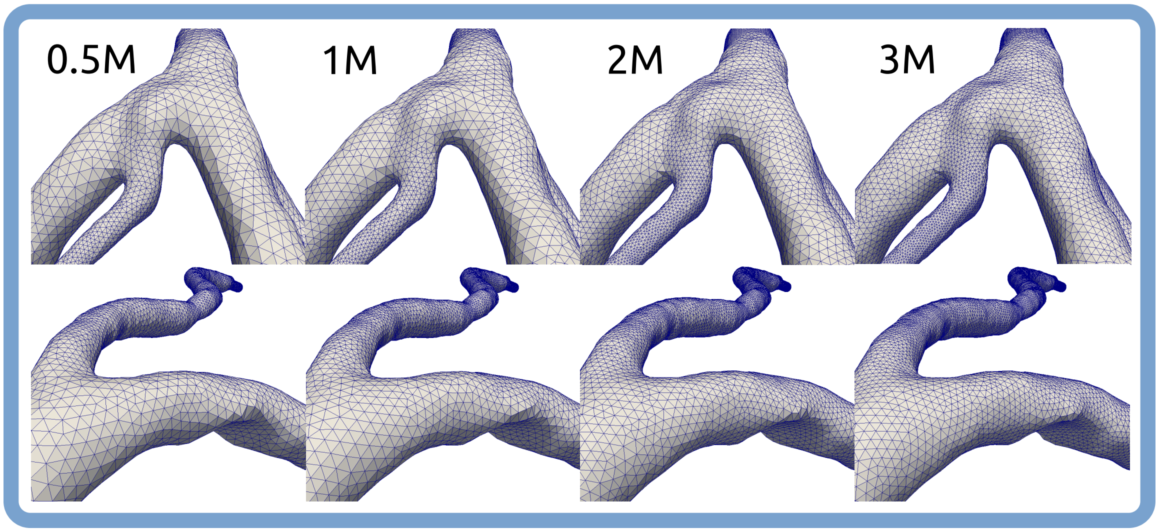

Figure 4.2.1: Snapshots of meshes with different refinement level from pilot 7 (upper row) and 5 (lower row).

Simulations were run for 10 cardiac cycles for pilot 5 and 7, and 5 cycles for pilot 2. Results from the last cycle were analyzed at outlets and interior locations. The mesh errors, as defined in equations (3.10) and (3.11), are plotted in figure 4.2.2, with numerical values in table 4.2.2.

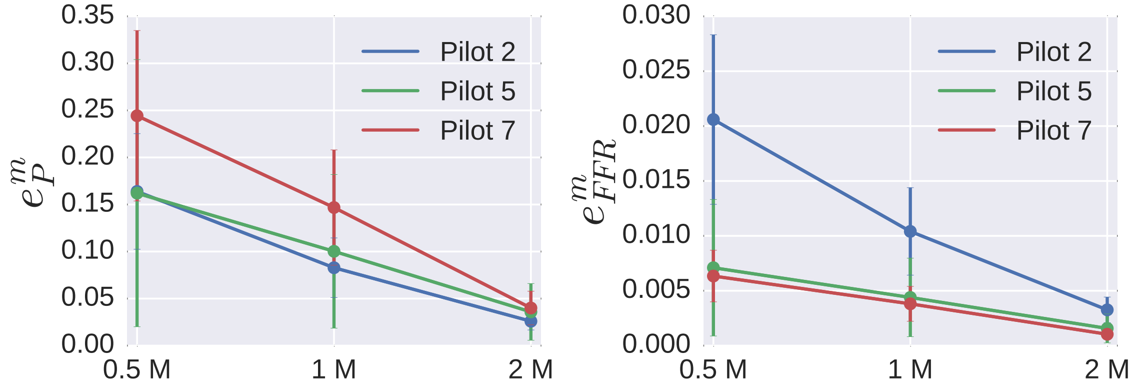

Figure 4.2.2: Comparison of mesh refinement levels. Mean errors with standard deviation.

Mesh	MAE	
	e_p^M	e_{FFR}^M
0.5M	0.190±0.038	0.011±0.007
1M	0.110±0.027	0.006±0.003
2M	0.034±0.006	0.002±0.001

Table 4.2.2: Mesh errors. Mean±SD over outlets and interior locations.

4.2.2 CONVERGENCE TO PERIODIC STATE

Simulations were run for 10 cardiac cycles to evaluate convergence on the 1M meshes of pilot 5 and 7. The residuals in pressure and FFR were computed at every outlet for each cycle, according to equations (3.13) and (3.14). Residuals for all transient simulations are plotted in figure 4.2.3.

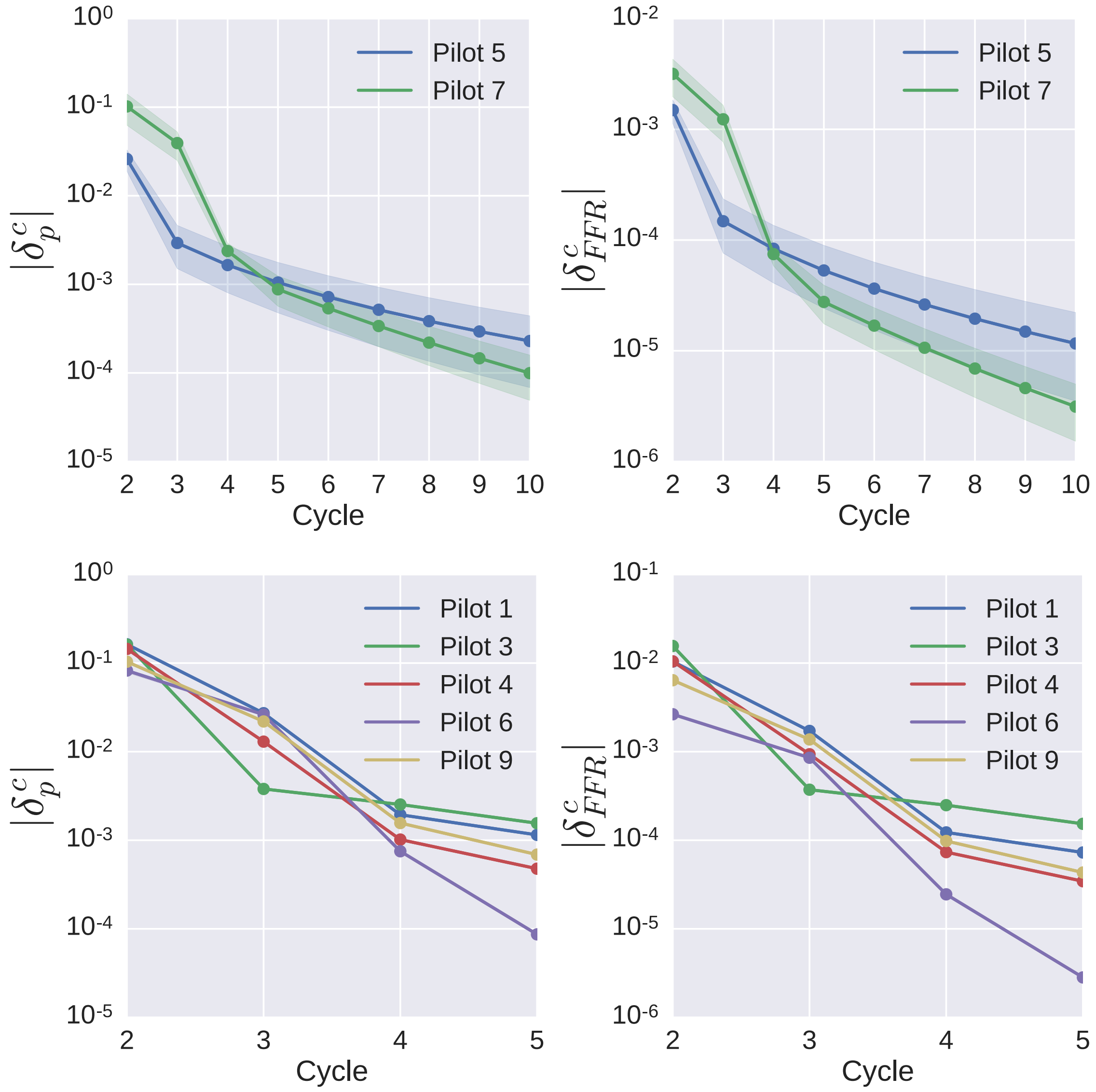

Figure 4.2.3: Convergence of transient simulations. Average outlet residual for all pilots (number of outlets as in table 4.1.2). Shaded areas are the 95 % confidence intervals.

Among all pilots, the maximal $|\delta_p^c|$ and $|\delta_{FFR}^c|$ the last cycle was $2.73 \cdot 10^{-3}$ and $2.30 \cdot 10^{-4}$ respectively. Steady simulations were all run for 1000 iterations. Convergence for all patients is shown in figure 4.2.4. Maximal residual the last iteration was $8.39 \cdot 10^{-6}$ in pressure and $1.27 \cdot 10^{-6}$ in FFR.

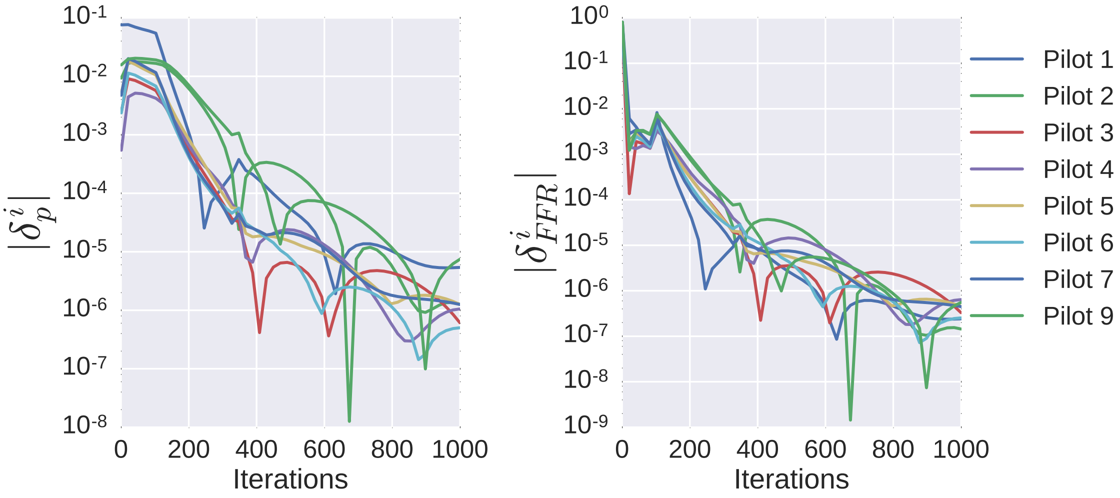

Figure 4.2.4: Average outlet residuals in pressure and FFR for all steady simulations, plotted every 20th iteration.

The difference between mean inlet flow and the sum of outlet flows (error in conservation of mass) was on average 0.047%±0.063% for transient simulations, and 0.049%±0.066% for steady simulations. The (decidedly) largest error in continuity was found in the transient and steady simulations of pilot 7, both with 0.2% difference between inlet and outlet flow.

4.2.3 STREAMLINE DIFFUSION COEFFICIENT

To evaluate the significance of the streamline diffusion coefficient *sdc*, simulations on the 1M mesh of pilot 5 were run with *sdc* = 1.0, 0.5 and 0.25. The errors relative to *sdc* = 0.25 were computed for the two other cases as described in 3.3. In figure 4.2.5, the mean errors are presented with standard deviation. The numerical values are given in table 4.2.3.

sdc	**MAE**	
	e_p^{sdc}	e_{FFR}^{sdc}
0.5	0.0517±0.0437	0.0024±0.0020
1.0	0.1335±0.1035	0.0068±0.0052

Table 4.2.3: Streamline diffusion error. Mean±SD over outlets and interior locations (n=14).

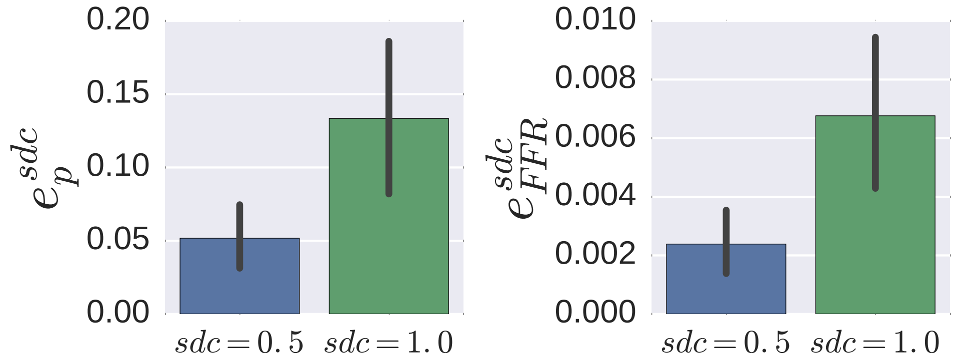

Figure 4.2.5: Effect of streamline diffusion coefficient. Mean error with SD.

4.3 Validation

The results were compared with other, physiologically validated simulation results of coronary flows. Figure 4.3.1 shows computed flow waveforms for pilot 5 together with model results by Kim et al. [65] and Taylor et al. [13], in addition to the simple cor-0D model results.

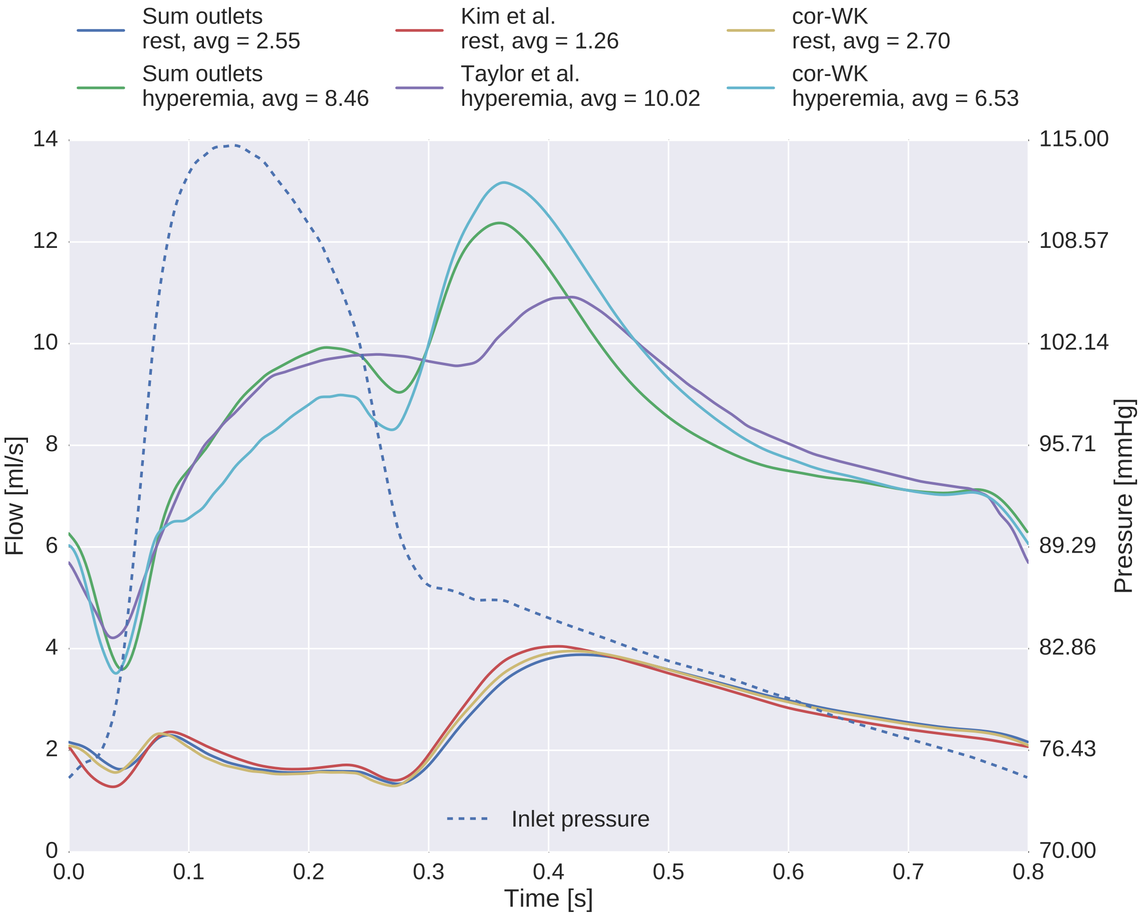

Figure 4.3.1: Comparison of flow waveforms with Kim et al. [65] and Taylor et al. [13], and the lumped parameter cor-0D model solutions. Sum outlets are the total flow out of the 3D domain of pilot 5, while references are waveforms for the LM coronary artery. Curves are scaled to the average flow rate of the corresponding 3D result (rest or hyperemic), for comparison of the shapes. True averages can be read from the legend ($[ml/s]$).

The models used by Kim et al. and Taylor et al. have been developed in the HeartFlow project, where simulations have been confirmed to replicate realistic coronary flows [70]. They also model coronary circulation with 3D CFD and cor-0D models at the outlets, but their comprehensive models further include the aorta and the RCA in the 3D model, and a lumped parameter heart model. The total outlet flow is plotted for each patient in figure 4.3.2.

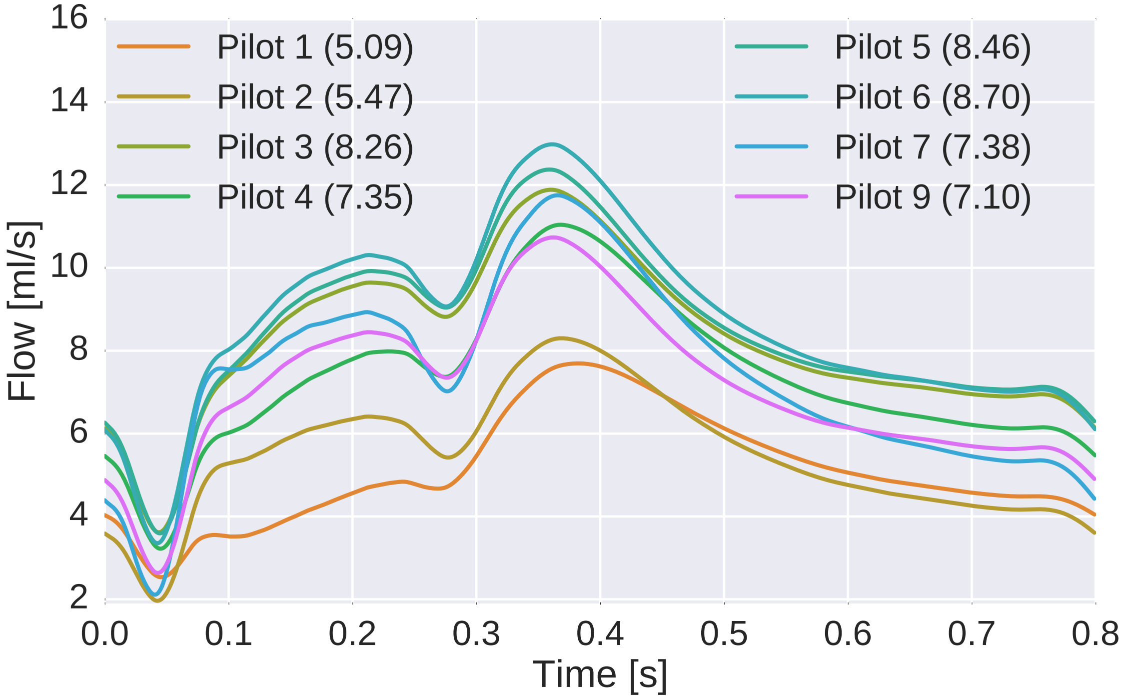

Figure 4.3.2: Sum of outlet flow for all patients. Cycle average flow rates in parentheses ($[ml/s]$).

In table 4.3.1 the minimal $\mathrm{FFR}_{\mathrm{CT}}$ for each patient is compared with clinically measured FFR (where available).

Pilot ID	**FFR**	**$\mathrm{FFR}_{\mathrm{CT}}$**		**Difference**	
		Transient	Steady	Transient	Steady
1	0.40	0.89	0.89	-0.49	-0.49
2	0.81	0.77	0.77	0.04	0.04
3	0.87	0.84	0.85	0.03	0.02
4	0	0.77	0.78	-	-
5	1	0.88	0.88	-	-
6	0.50	0.91	0.91	-0.41	-0.41
7	0.89	0.95	0.95	-0.06	-0.06
9	1	0.92	0.92	-	-

Table 4.3.1: Comparison of minimal $\mathrm{FFR}_{\mathrm{CT}}$ with clinical FFR from ICA. 0 signifies total occlusion, and 1 means no ICA was performed (diagnosed healthy from CT images).

The flow was evaluated through some prominent stenoses, of pilots 1, 2, 4 and 5. Stenotic Reynolds (Re) and Womersley (Wo) numbers were computed (the radius of a stenosis was computed as $r_s = \sqrt{A_s/\pi}$, where A_s is the stenotic area).

Pilot	*%stenosis*	$r_s[cm]$	Re_D^s	$Re_{D,max}^t$	Wo
1	75	0.10	570	841	1.74
2	70	0.07	593	845	1.36
4	65	0.06	444	618	1.13
5	25	0.15	112	152	2.68

Table 4.3.2: Evaluation of prominent stenoses in pilots 1, 2, 4 and 5. r_s is the stenosis radius. Stenosis degree is given in percent reduction in original lumen area. Re_D^s and $Re_{D,max}^t$ are the steady and maximal transient mid-stenotic Reynolds numbers, defined in equation (2.12). Wo is the Womersley number, defined in equation (2.13), for the primary harmonic of the pulsatile flow ($\omega=2\pi/T$).

Finally, stenotic velocity profiles and post stenotic streamlines were inspected, shown in figure 4.3.3 and 4.3.4.

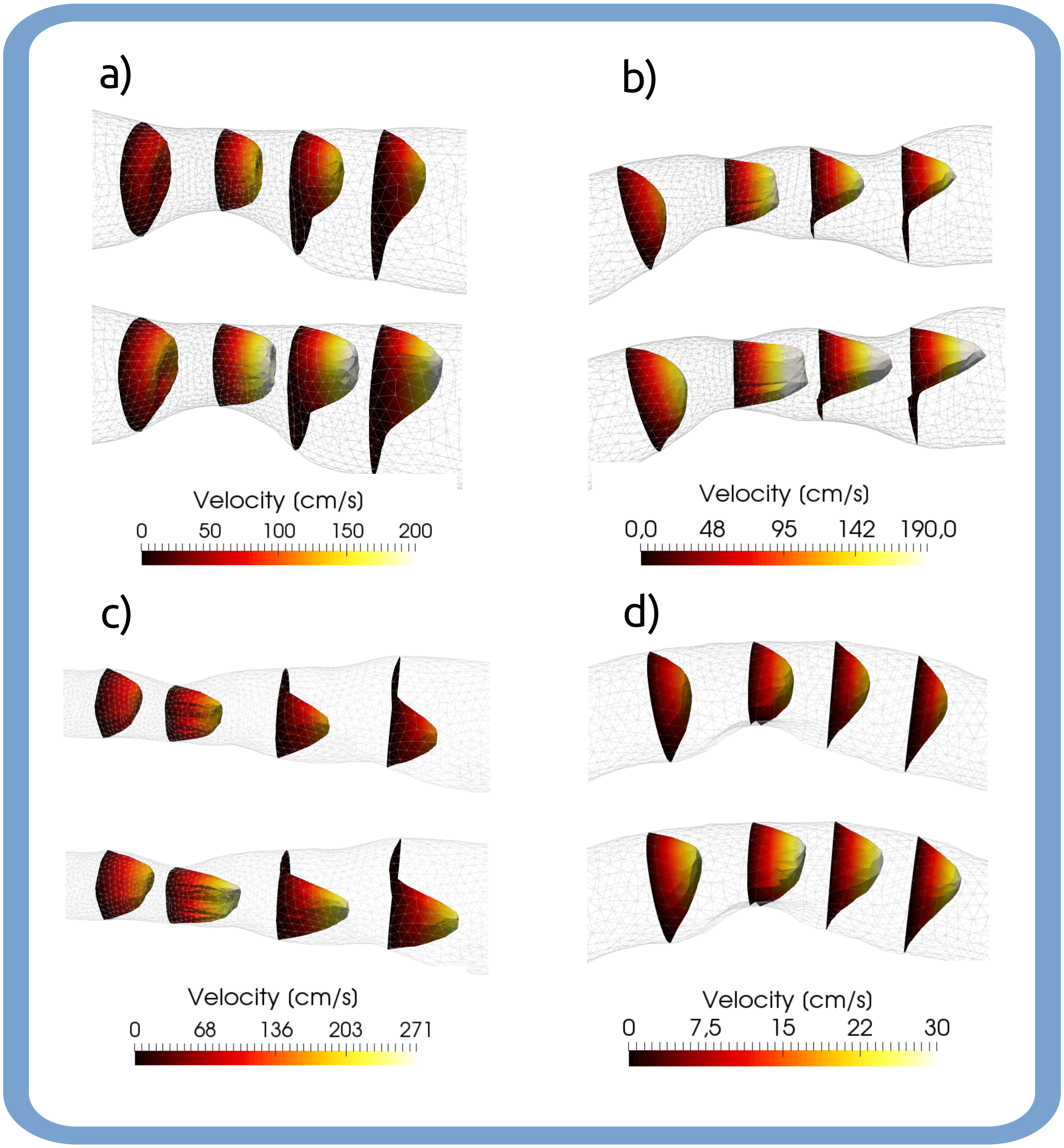

Figure 4.3.3: Velocity profiles through stenoses of pilots a) 1, b) 2, c) 4 and d) 5. Steady solution (upper profiles) and maximal transient profiles (lower).

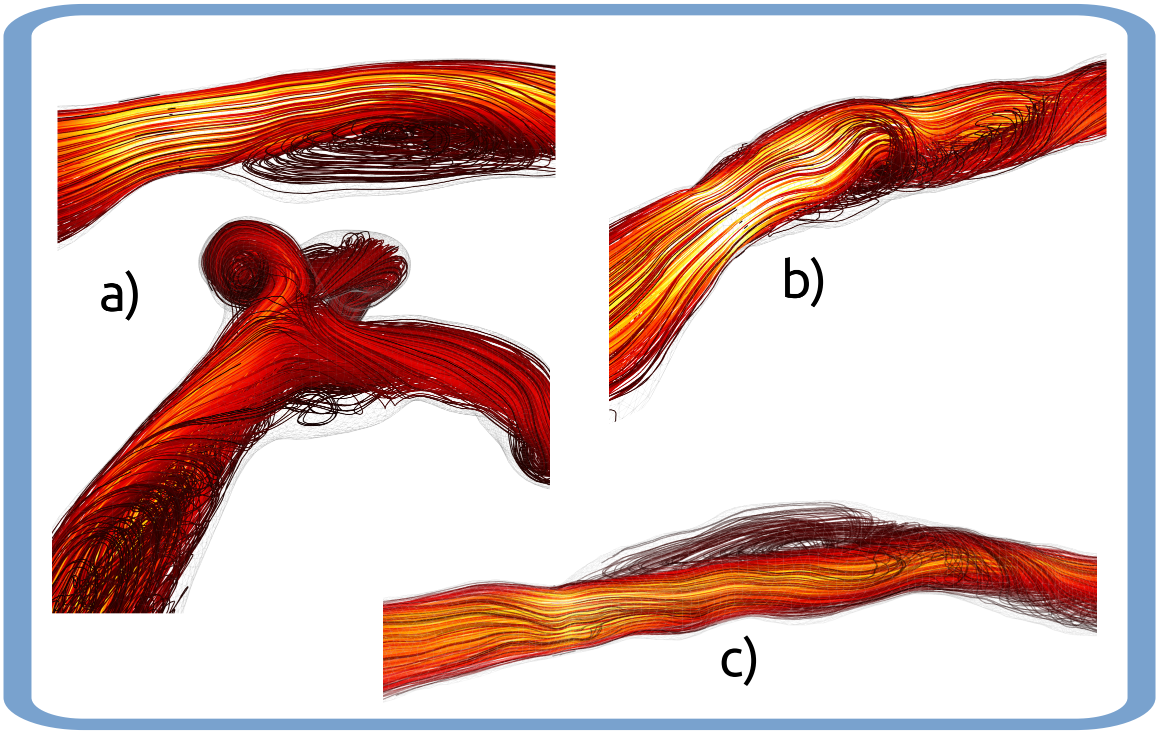

Figure 4.3.4: Streamlines dowsntream of stenoses in pilots a) 1, b) 2 and c) 4.

4.4 Comparison of Transient and Steady Simulations

Transient and steady simulations were run on the 8 patients listed in table 4.1.3, applying the meshes in table 4.1.2. The simulations followed the setup presented in 3.1, using the patient-specific parameters in table 4.1.3 as described in 3.2.2. Transient simulations were run with a time step $\Delta t = 0.001$ *s*, except from pilots 4 and 6, where 0.0005 *s* was required for convergence. All steady simulations had Δt= 0.0001 *s*. Convergence of the transient simulations was supported in residuals, being < 10^{-2} and 10^{-4} in outlet pressures and FFR respectively for the the last cycle (residuals are defined in 3.3). Similarly, steady simulations had residuals < 10^{-5} and 10^{-6} the last iteration. Numerical streamline diffusion coefficient was set to 1.0 in all simulations.

Pressures and FFR were computed and compared at interior locations (n=30) and outlets (n=61), as outlined in section 3.5. Normality of the distributions of e_p^s at outlets and interior locations (and all combined) was tested with the *Shapiro-Wilks* test, resulting in a scores W=0.94 and W=0.98 (W=0.96), p=0.005 and p=0.74 (p=0.01). Similarly, normality tests for e^s_{FFR} gave W=0.93 and W=0.89 (W=0.93), p=0.006 and p=0.004 (p=0.0002) for outlets and inlets (and all combined) respectively. Difference in interior and outlet error distributions was further tested by the *Mann-Whitney U* test for non-parametric distributions, resulting in U=961 (p=0.90) and U=1003 (p=0.64) for errors in FFR and pressure respectively. In the subsequent analysis, all errors are treated as coming from one population.

Mean average errors (MAE) and RMSE were computed per patient, with errors defined in equations (3.15). Results are shown in table 4.4.1. By definition, $e^s_{P,i}$ is the relative error in pressure (relative to the average 3D inlet-outlet pressure drop), and the $e^s_{FFR,i}$ is the absolute error in FFR.

Pilot		**FFR^t$_{\mathrm{CT}}$**	**MAE**		**RMSE**	
ID	$n_{loc}(n_o + n_i)$	$n = n_{loc}$	e^s_p	e^s_{FFR}	e^s_p	e^s_{FFR}
1	8 (5+3)	0.93±0.03	0.0297±0.0193	0.0019±0.0012	0.0354	0.0022
2	8 (5+3)	0.87±0.06	0.0240±0.0115	0.0031±0.0015	0.0263	0.0034
3	12 (8+4)	0.92±0.04	0.0152±0.0068	0.0015±0.0007	0.0167	0.0016
4	10 (7+3)	0.93±0.07	0.0211±0.0229	0.0015±0.0016	0.0311	0.0022
5	16 (11+5)	0.96±0.03	0.0129±0.0129	0.0007±0.0007	0.0172	0.0009
6	11 (8+3)	0.97±0.02	0.0183±0.0222	0.0006±0.0007	0.0263	0.0009
7	17 (11+6)	0.97±0.02	0.0338±0.0321	0.0011±0.0010	0.0362	0.0011
9	10 (6+4)	0.95±0.02	0.0177±0.0055	0.0011±0.0003	0.0186	0.0012

Table 4.4.1: Errors of the steady simulations, as compared with transient solutions. n_{loc} (n_o+n_i) is the number of locations (outlets+interiors). $Mean(FFR^t_i)$±SD is reported for each patient. The MAE are in $mean(|e^s_{P/FFR}|)$±SD, and RMSE are in mean.

Mean FFR of the patient sample was 0.94±0.03. The average mean error in pressure was 0.0216±0.0072 (2.16% of the average pressure drop). Similarly, MAE in FFR was 0.0014±0.0008 across patients. In comparison, average RMSE is 0.0260±0.0079 and 0.0017±0.0009 in pressure and FFR respectively.

Combining all patient locations into one sample, the MAE in pressure was 0.0216±0.0203, and

RMSE was 0.0269. Taking the direction of the errors into account, mean e^s_P was -0.0176. Similarly for FFR, MAE was 0.0013±0.0013, RMSE=0.0017 and with direction, mean error is -0.0012. All location errors $e^s_{P,i}$ and $e^s_{FFR,i}$ are plotted versus FFR^t_i in figure 4.4.1. Outlet errors are also plotted versus the local Womersley number in figure 4.4.2.

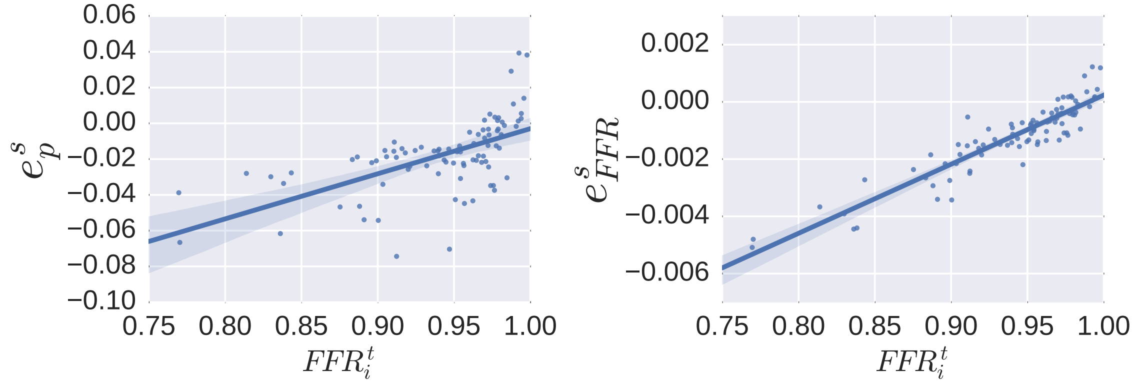

Figure 4.4.1: Plot of steady errors versus FFR, with least squares linear regression of FFR errors. The shaded area is the 95 % confidence interval for the regression line.

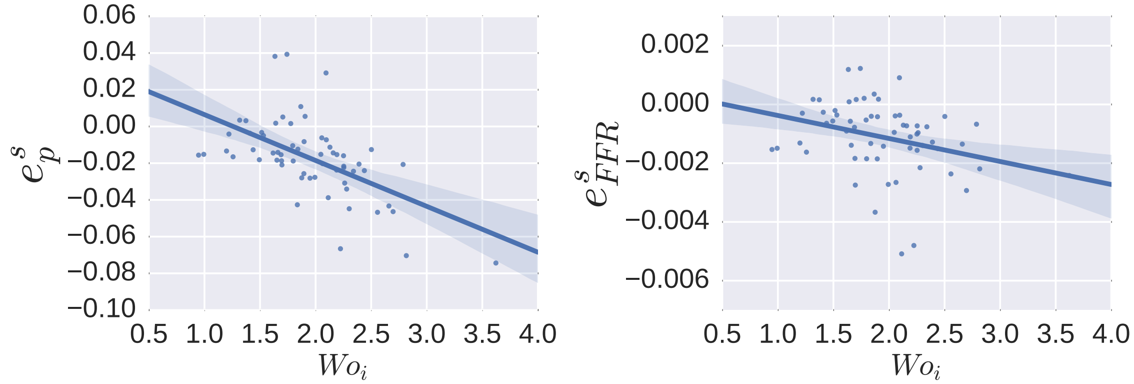

Figure 4.4.2: Plot of steady errors versus local Womersley number, with least squares linear regression of the errors. The shaded area is the 95 % confidence interval for the regression line.

The correlation between FFR^t_i and the errors was analyzed. *Spearman′srho* was 0.67 for e^s_P, and 0.90 for e^s_{FFR} (all p<0.001). Similarly, correlation with *Wo* gave *Spearman′srho* -0.59 (p=<0.001) and -0.36 (p=0.004) for pressure and FFR errors. Least squares linear regression gave the following relation between the steady FFR-error and FFR

$$e^s_{FFR,i} = -0.0239 + 0.0241 \cdot FFR^t_i, \tag{4.2}$$

with standard error 0.0011 (p<0.001).

The largest error (in magnitude) in FFR was -0.0051, found in pilot 2. Maximal sampled errors are listed for each patient in table 4.4.2, along with their respective FFR^t (which coincide for maximal errors in FFR and pressure in all cases). The patient average max errors were 0.0504±0.0193 in pressure and 0.0017±0.0009 in FFR.

Pilot ID	FFR^t	$\max(\lvert e^s_P \rvert)$	$\max(\lvert e^s_{FFR} \rvert)$
1	0.90	0.0543	0.0034
2	0.77	0.0388	0.0051
3	0.84	0.0277	0.0027
4	0.77	0.0666	0.0048
5	0.88	0.0467	0.0024
6	0.91	0.0744	0.0024
7	0.95	0.0704	0.0022
9	0.92	0.0240	0.0015

Table 4.4.2: Maximal errors of steady simulations, as compared with transient solutions. FFR^t is the transient FFR value at the location where the maximal error is sampled.

The average steady error in outlet flows were computed for each patient, according to equation (3.17). For all patients, the mean error in flow was -0.139%±0.102%, with the largest error in magnitude found in pilot 2, -0.348%.

5

Discussion

This chapter contains a profound discussion of applied methods and results presented in the preceding chapters. The chapter is divided into two sections. The first is dealing with the discussion of methods and models applied, regardless of the outcome of the results. The second discuss results, models and methods enlightened by the findings of the previous chapter.

5.1 On the Methods

The applied methodology for constructing patient-specific 3D domains is very susceptible to fallacies made by the operator. In this respect, the correct capture of critical stenoses and branching vessels is at the mercy of the operator's abilities to interpret the CT images. Another limitation lays in the mesh generation methods. For compatibility with the solver (FEniCS), no inflation layers were created from the vessel walls. It is desirable with higher mesh refinement in the normal direction from walls, due to high velocity gradients in the boundary layers. Without mesh inflation layers, the viscous losses in the proximity of the walls may be underestimated. This is of importance for the comparison of pulsatile and steady flows, as stenotic wall shear stress is particularly affected by oscillating flows [71]. Yet, the verification of mesh refinement outlined in 3.3 aims at quantifying the errors caused by the mesh, and thus diminish its significance in the CFD solutions.

The presented approach for tailoring simulations to patient-specific parameters is incomplete. SBP values applied were based solely on brachial pressure, which is shown to be 8-10 *mmHg* lower than systolic aortic pressure [72]. Total coronary compliance was assumed equal in all patients, as well as the rheological parameters of blood, and LCA flow was approximated to 2% of cardiac output in all patients. And most notably, the hyperemic conditions were based on the assumption of a universal fourfold increase of baseline coronary flow. However, the primary goal of this thesis is not to predict real FFR as accurately as possible, but to investigate differences in transient and steady simulations of physiological, hyperemic coronary flows. Thus, emphasis was put on developing physiologically reliable models, sufficient for such an analysis. There are still some milestones to reach until perfectly tailored models can be feasibly integrated in the presented methodology.

Previous studies do not agree if heart rate increases during adenosine induced hyperemia. Wilson et al. reported no significant changes in heart rate [27], while others have suggested 15-20% increase [29, 73]. As the primary goal of this thesis is to assess the difference between time averaged transient and steady simulations, pulsatile features are of obvious interest. From oscillatory flow theory, velocity patterns deviate more from steady solutions with increasing Womersley number [74]. The conservative approach for evaluating the error of a steadiness assumption would seek to maximize oscillatory characteristics of the transient flows, and thus maximize the Womersley number (within a physiological range). In the present work, this is approached by increasing the mean baseline heart rate with 25% giving an average hyperemic period of 0.8 *s*, as an estimated lower bound for the mean period of the population. Due to the lack of conformity in research on hyperemic heart rate, this estimate was used in all patient simulations. Furthermore, clinical studies have shown that FFR does not change significantly despite as much as a 40% increase in heart rate [75, 76].

Few studies have addressed the validity of modeling vessel walls as rigid in coronary flow simulations. Findings by Malvè et al. show that for the computation of wall shear stress (WSS), rigid walls introduce significant qualitative and quantitative errors [77]. However, Morris et al., state that *"(...) there is no strong evidence that it is necessary to represent the motion or compliance of the vessel"* for the computations of virtual FFR, yet without citing any studies [50]. The presented methods rely on the validity of the rigid wall assumption in the 3D domain. More complex fluid-structure interaction models were regarded as too comprehensive for the scope of this thesis. However, reduced order models (1D or 0D) could perhaps incorporate the arterial compliance more feasibly, and evaluate the rigid wall assumption.

5.2 On the Results

5.2.1 Patient-specific Models

Judging the physiological resemblance of the created patient-specific LCA geometries is beyond the scope of this thesis. Yet, it is suspected that the lack of experience with cardiology and CT images can have caused geometrical artifacts, including misinterpretation of stenoses and missing branches. Despite this, these are not expected to significantly affect the comparison results of steady and unsteady flow simulations. It is however, in the context of using FFR_{CT} for diagnosis, a weakness that the presented methodology for making geometries from CT images involves several manual tasks requiring profound knowledge of CA physiology and pathology. Geometrical disagreement is a considerable challenge, as both uncertainty in stenosis radii and missing branches downstream of stenoses have a pronounced effect on the computed FFR [49].

5.2.2 Verification

The mesh study gave conforming results across the three patients studied, despite different setup for updating total resistance. As the error in FFR of the 1M meshes was (on average) less than 0.007, below the level of importance in a diagnostic context [78], this refinement level was chosen for the subsequent simulations. In addition, simulations on 1M meshes were considerably more feasible than the finer meshes regarding computation time. Although the 2M mesh showed less discrepancy with the 3M results (as expected), the choice of a 1M mesh was not expected to have decisive effect in the comparison study of steady and transient simulations.

The 10 cycle simulations on pilot 5 and 7 indicated that 5 cycles would be sufficient for convergence in cyclic average pressure and FFR, with residuals reaching 10^{-3} and 10^{-4} respectively. In subsequent 5-cycle simulations, these limits were not significantly exceeded. Steady simulations had even better convergence, with all residuals $<10^{-5}$. The number of iterations could have been reduced to the half (500) without losing accuracy compared with 5 cycle transient simulations. Conservation of mass was <0.05% of the flow rates on average. The maximal of 0.2% error for pilot 2 is high, and may have a significant effect on the computed pressure results. The cause for these errors are suspected to be associated with the mesh refinement level. Still, since the mesh error in FFR was judged to be sufficiently small, the continuity error was not suspected to contribute significantly to the FFR results.

The streamline diffusion coefficient was set to 1.0 in the final simulations. The results from one patient gave indications that this would yield in an unimportant error in FFR (<0.01). This error was not expected to have influence on the comparison study of transient and steady simulations, by the same arguments as stated in the discussion of the mesh verification. However, only one patient geometry was studied, so the error may be different for the others.

5.2.3 VALIDATION

The model results are in good agreement with previous work and physiologic coronary flow patterns. The average flow rates are within normal range of baseline or hyperemic LCA flow rates [27, 28]. Furthermore, the model evidently reproduces characteristic coronary flow patterns, with suppressed flow during systole which increase in diastole. For hyperemic conditions, this pattern is less prominent, in agreement with simulation results of Taylor et al. [13]. It is expected that a correct representation of the oscillatory patterns in the flow waveforms has a direct impact on the time average pressure drop. This statement is based on the fundamentals in oscillatory flow theory, where the relation between flow rate and pressure gradient is governed by the amplutides and periods of the waveform harmonics [74]. The simulation results are qualitatively similar in all patients, with no conspicuous instance in either flow, pressure or FFR.

The computed FFR results deviate from to the corresponding clinical FFR measurements. Although some simulations show good agreement, the differences between measurements and computations are spanning from 0.03 to 0.5, with simulations over-predicting FFR. Furthermore, the fairly good agreement in some patients might just as well be luck, or a fortunate combination of parameters, rather than accuracy. It is not in the main objectives of this thesis to replicate clinically measured FFR. However, the following discussion may be valuable to the further development of the presented models and methods. There are particularly two aspects suspected to be the cause of these errors. One lies in errors in post-stenotic resistance. Missing daughter branches in the coronary tree would increase the peripheral resistance of a stenotic mother branch, as there are too few resistances in parallel downstream of the stenosis. This would lead to an underestimation of the flow in the critical branch, thus limiting the stenotic pressure drop, being proportional to flow rate squared over severe stenoses [24]. In addition, distribution of terminal resistances is a source of error. Based on the general Murray's law, outlet resistances are assumed to be inversely proportional to the terminal radius cubed. Considering the fact that outlet radii are products of the semi-manual segmentation process make results highly sensitive to operator skills. Furthermore, Murray's law is based on an idealization of physiology, which is an oversimplification of real arterial trees [56, 57].

The other main cause is suspected to be the approximation of hyperemic flow rate in the LCA itself. This relies on rough estimates of both coronary flow fraction of cardiac output and the hyperemic conditions. More advanced methods exist, such as estimating flow based on allometric scaling laws, relating cardiac mass with flow [79]. Such methods were not applied in this work, partially due to limited patient material. Another potential remedy to uncertainty in hyperemic flow is the use of novel Doppler-ultrasound techniques to measure coronary flow rates non-invasively [52]. This is under development at NTNU, and is a promising way to enhance the presented models further.

Many researchers agree that correct representation of coronary geometry and hyperemic flow is crucial for the success of $\mathrm{FFR}_{\mathrm{CT}}$ as a diagnostical tool [13, 49, 50]. These challenges are universal, and beyond the scope of this thesis to discuss further. Still, the results obtained in the present work are promising, despite limited extent in the patient-specific tailoring of models.

The comparison of steady and transient velocity profiles does not give any indication of salient unsteady features in the profiles. However, they indicate separated flow and obvious deviations from parabolic profiles in post-stenotic regions. There are also prominent secondary flows and rotations in the flow fields, with large vortices downstream of stenoses. Nonetheless, previous studies have shown that reduced order models (1D or 0D) of coronary flows are comparably accurate for calculations of pressure drop [54, 80]. Hence, it may not be necessary to account for suchlike multidimensional features in the assessment of FFR, except from through lumped descriptions of their bulk behavior.

Stenotic pressure losses are strongly associated with the expansion of flows, where turbulence may occur in severe stenoses [24]. However, separated flows may be still laminar, despite strong rotation. Reynolds numbers in the simulated flows are low compared with typical transition values in hemodynamical flows of $\sim$2200 [23], justifying the exclusion of turbulence models in the numerical methods. Furthermore, the Womersley numbers computed at severe stenosis locations were low (<2.7), giving indications of quasi-steady flow regime in these locations [71].

5.2.4 Comparison of Transient and Steady Simulations

In the preceding chapter, the discrepancy in steady and transient results was denoted the (steady) error, with the transient solutions being regarded as the ground truth. This notation will be applied in the following discussion. Absolute errors in FFR and relative errors in pressure were assessed. The errors were sampled at several locations within each patient geometry, and were assessed both on a per-patient level and as all sampled errors combined.

The error distributions were not found to be highly skewed, yet significantly different from a normal distribution ($p<0.05$). As a consequence, normality was rejected and non-parametric tests were used in subsequent statistical analyses. Errors sampled internally in the 3D domain and at the outlets were not found to be significantly different with the *Mann-Whitney U* test ($p>0.6$), and were therefore treated combined.

The mean patient error in FFR was 0.0014±0.0008 (units FFR), and in relative pressure error 0.0216±0.007 (or 2.16% of the average patient 3D-model pressure drop). There were no big differences in evaluating the errors from the patient means or the means of the whole population of sampled errors. All errors in FFR were remarkably lower than the relative pressure errors. This is obvious from the fact that FFR is distal pressure normalized to a high inlet pressure, whereas the absolute pressure error was normalized to the much lower average inlet-to-outlet pressure drop. The latter choice was motivated by how errors in pressure should be interpreted: Since the absolute pressure level is irrelevant for the (incompressible) flows, a much more meaningful value for normalization was found to be the 3D pressure drop. Since errors in pressure and FFR both derive from deviations in steady and transient pressure, they are intrinsically biased. For the purpose of evaluating errors relevant in a clinical context, FFR-errors are given the most attention in the following.

Except from a few locations with high FFR values, steady simulations overestimate FFR compared with unsteady simulations (i.e. underestimate the pressure drop). There were found strong and significant correlations between FFR and the steady errors, being most pronounced in the absolute error in FFR (*Spearman's rho* = 0.90, p<0.001). The error in FFR is shown to be increasing with decreasing FFR in a linear relationship given in equation (4.2). This has implications for the evaluation of the errors, as the mean error is not representative for the error in the critical range of FFR. The correlation between errors and local Womersley number was much weaker, yet statistically significant (p<0.01). However, on the basis of the presented findings, Womersley number is not expected to have strong predictive power in the assessment of errors caused by a steady flow assumption.

This linear relationship is reasonable from a physical point of view. If there is a systematical difference in steady and time averaged pressure gradient, this difference would accumulate in the pressure drop. Higher pressure drops, would give higher absolute errors in pressure, and higher pressure drops give lower FFR. Thus, if there would be a constant difference between steady and transient pressure gradients, there would be a linear relationship between FFR error and FFR. The resulting difference in pressure gradient would further lead to a difference in flow rate, which is observed in an average difference in outlet flow of 0.139% between steady and unsteady simulations.

The average root mean square error in FFR is 0.0017±0.0008 over the patient sample, which is higher than the average mean absolute error. As the RMSE gives a higher penalty to errors of larger magnitude, this indicates that large errors are not well represented in the mean error. Since the power of FFR as an index lays in its reliable cut-off value to signify severe stenoses [7], errors associated with FFR of 0.75-0.80 are of particular interest. Maximal error in FFR per patient was on average 0.0017±0.0009, with the single highest value 0.0051. Invasively measured FFR is reported with two significant figures. Hence, an error of 0.005 in FFR can be suspected to determine the diagnosis outcome, due to round-off error. However, the uncertainty in clinical FFR is in the same order of magnitude. Studies by Berry et al. have reported that the repeatability of invasive FFR is high, with a mean difference of ±0.04 in FFR between two consecutive ICA procedures on the same patient [78]. These results are supported by others, finding coefficients of variation (standard deviation over mean) of 2.5-4.2% [76, 81]. In this regard, the absolute maximal steady error is still <25% of the repeatility errors of invasive FFR procedures, and the mean FFR error <10%. The steady error in FFR_{CT} is therefore not likely to be decisive for clinical intervention.

The findings of small deviations in FFR between steady and transient coronary flow is in agreement with previous studies. Through *in vitro* experiments, Mates et al. concluded that stenotic coronary flow is quasi-steady in behavior [20]. Huo et al. found, also through *in vitro* experiments, that the error in pressure drop was <5% when comparing steady and pulsatile flows through artificial coronary stenoses [19]. The only known study addressing the validity of steady 3D flow simulations to derive FFR_{CT}, by Bulant et al. [21], is also in agreement with the present work. They reported a mean error in FFR of 0.9%±1.2%. In the more detailed treatment in his unpublished doctoral thesis, Bulant reports a mean error of 0.004±0.005 in FFR, and mean relative error of 0.036±0.016 in pressure [58], which are slightly higher than the mean errors found in this study. As a distinction from the present work, Bulant et al. assessed errors averaged over large vessel segments. By such a method, internal variations in the steady error within one patient geometry would be averaged out by the global mean error. A combination of such a volume-averaging evaluation of errors and the present approach applied to several distal segments in each branch is a third option. By doing so, the evaluation of errors could be assessed per sub-domain, and not per vessel or per specific location, as in the aforementioned and present approach respectively. Consequently, internal relations between steady error and FFR could be analyzed on a stronger statistical basis than what is done in the present study.

Although in good agreement with related work, there are certain aspects with the present results that are disputable. Steady FFR errors are in the same order of magnitude as the mesh and numerical diffusion error, and acting in opposite directions. Although equal meshes and streamline diffusion coefficient values are used in transient and steady simulations, their associated numerical errors may not be equal. If in fact the assumed numerical errors are significantly lower in the steady simulations, this may affect the comparison results, leading to underestimated FFR errors. The mesh refinement level was chosen on the consideration that the associated errors were insignificant to the computed FFR values in a clinical context, and due to practical limitations set by moderate computational resources. Numerical streamline diffusion was desired due to instability problems in early simulations. In hindsight of the comparison results, it would have been desirable with a lower criteria for verification errors, as it is not known if these are equal in steady and transient simulations.

In spite of this, the present work inevitably reveal small differences between steady and unsteady simulations in FFR_{CT}, and it is not expected that refining the numerical methods would affect the main conclusions of this thesis. Other errors in the model are evidently much larger, which is seen from the comparison of computed and measured FFR. Uncertainty in patient parameters, geometry and distriubution of resistances are expected to be much more influential on the computed FFR results than the steadiness assumption. State-of-the-art FFR_{CT} researchers have developed models which are performing well for diagnosis, yet with 0.06 (Morris et al. [16]) and 0.03 (HeartFlow [15]) mean difference between FFR_{CT} and invasive FFR. In comparison, steady errors are negligible. As a summary of the preceding discussion, it can be concluded that the errors introduced by assuming steady conditions in coronary flow simulations are insignificant for the assessment of FFR.

6

Concluding Remarks

This chapter recapitulates the main constituents of the three preceding chapters. The work is summarized in the first section. In section 6.2, the concluding remarks from the discussion in the previous chapter are stated. Finally, limitations of the study are identified and directions for further work are suggested.

6.1 SUMMARY OF THE WORK

This thesis is concerned with patient-specific CFD simulations of coronary blood flow for the assessment of FFR and coronary artery disease. Patients recruited in NTNU's ongoing FFR_{CT} research project were processed in silico using a combination of open source and preliminary inhouse software utilities. The work presented has been highly integrated in the parallel progress of the research project. Through continuous validation of models and implementations, the documented methods and results have contributed to developments in the project.

Patient-specific models were constructed from material provided by clinicians at St. Olavs Hospital, Trondheim. Steady and transient flow simulations were conducted on 8 patients, with the aim of quantifying discrepancies in $\mathrm{FFR_{CT}}$ results. For the purpose of verifying the computational methods, the effect of mesh refinement level, periodic convergence criteria and numerical diffusion was inspected. In addition, the validity of the CFD results was assessed through validation of the physiological and physical features of the solutions. Finally, the results obtained from steady and transient simulations were compared and analyzed, leading up to a discussion on the applied methods and major findings.

6.2 CONCLUSION

The computational model applied and developed during this work resembles physiological coronary flows, and is in agreement with comparable state-of-the-art simulation models.

The mean difference in $\mathrm{FFR_{CT}}$ from steady and unsteady flow simulations was 0.0014 ± 0.0008 units FFR, well below the deviations in repeated invasive FFR procedures of $\sim$0.02-0.04. Furthermore, there was found a strong and linear relationship between FFR and the steady error with the applied methodology, with larger steady errors occurring at locations with low FFR values.

Although maximal deviations between steady and unsteady computed $\mathrm{FFR_{CT}}$ reach the order of the clinical measurement precision (0.005), these are not expected to have decisive action for clinical intervention.

Per patient comparison of clinical FFR and $\mathrm{FFR_{CT}}$ show promising results. Still, agreement is only seen occasionally, with pronounced errors on certain patients. The presented methods for tailoring the computational model to patient specifications is sufficient for a comparison of steady and unsteady simulations of physiological coronary flows, but further development is required to adequately reproduce invasive FFR for clinical applications.

Based on the findings of this work, simulation of steady flow conditions introduce insignificant errors for the assessment of $\mathrm{FFR_{CT}}$.

6.3 LIMITATIONS

This study is confined to investigate flows only in LCAs, and not the RCAs. This can be justified from an argument that unsteadiness is more prominent in the LCAs due to the high influence of LV pressure counteracting systolic flow. However, the decision is based primarily on the need to limit the scope of this work. A complete investigation of the coronary arterial tree could either substantiate or question the conclusions made.

The verification of mesh refinement and streamline diffusion coefficient was only performed on transient simulations. These sources of errors may be different in steady and unsteady flows. Since the mesh and numerical diffusion errors are in the order of the steady errors, a complete verification of steady simulations would reveal the difference in steady and transient numerical errors.

The population sample of this work is limited in extent, both with respect to the number of patients and the span of FFR, concentrated around higher values. A larger group of patients would strengthen the statistical foundation of the presented results.

6.4 SUGGESTIONS FOR FURTHER WORK

In subsequent work following directly in the track of this work, the following topics are of high relevance:

- Investigate the difference in numerical errors for steady and transient simulations
- Expand the current study with more patients and a broader span of FFR
- Compare steady and unsteady flows when matching inlet flow rate instead of pressure

More universally, computational assessment of FFR have several other challenges to manage. One of particular relevance in this project is the semi-manual segmentation process. Future studies should aim at developing automated segmentation processes not requiring operator interference, and being able to manage variable CT image quality.

The problem with uncertainty in hyperemic conditions should be addressed, with an investigation of the potential for Doppler-ultrasound flow measurements to be used in tailoring patient-specific models. The present models can easily be adjusted to be used with flow rates as inlet conditions.

Reduced order models (0D and 1D) may further lower the computational expenses. In addition, such models may be used to inspect the significance of the rigid wall assumption by introducing arterial compliance in the models. Since the apparent difference between 3D and 0D model characteristics is small in this work, reduced order models may be a prospering direction for future work.

References

[1] Dariush Mozaffarian, Emelia J. Benjamin, Alan S. Go, Donna K. Arnett, Michael J. Blaha, Mary Cushman, Sandeep R. Das, Sarah de Ferranti, Jean-Pierre Després, Heather J. Fullerton, Virginia J. Howard, Mark D. Huffman, Carmen R. Isasi, Monik C. Jiménez, Suzanne E. Judd, Brett M. Kissela, Judith H. Lichtman, Lynda D. Lisabeth, Simin Liu, Rachel H. Mackey, David J. Magid, Darren K. McGuire, Emile R. Mohler, Claudia S. Moy, Paul Muntner, Michael E. Mussolino, Khurram Nasir, Robert W. Neumar, Graham Nichol, Latha Palaniappan, Dilip K. Pandey, Mathew J. Reeves, Carlos J. Rodriguez, Wayne Rosamond, Paul D. Sorlie, Joel Stein, Amytis Towfighi, Tanya N. Turan, Salim S. Virani, Daniel Woo, Robert W. Yeh, and Melanie B. Turner. Executive summary: Heart disease and stroke statistics—2016 update. *A Report From the American Heart Association*, 133(4):447–454, 2016.

[2] World Health Organization (WHO). Disease and injury regional mortality estimates, 2000-2012. `http://www.who.int/healthinfo/global_burden_disease/estimates/en/index1.html`, 2012. [Online; accessed 06.06.17].

[3] William F Fearon, Alan C Yeung, David P Lee, Paul G Yock, and Paul A Heidenreich. Cost-effectiveness of measuring fractional flow reserve to guide coronary interventions. *American Heart Journal*, 145(5):882 – 887, 2003.

[4] James K. Min, Charles A. Taylor, Stephan Achenbach, Bon Kwon Koo, Jonathon Leipsic, Bjarne L. NÃ¸rgaard, Nico J. Pijls, and Bernard De Bruyne. Noninvasive fractional flow reserve derived from coronary {CT} angiography: Clinical data and scientific principles. *JACC: Cardiovascular Imaging*, 8(10):1209 – 1222, 2015.

[5] Mark A. Hlatky, Akshay Saxena, Bon-Kwon Koo, Andrejs Erglis, Christopher K. Zarins, and James K. Min. Projected costs and consequences of computed tomography-determined fractional flow reserve. *Clinical Cardiology*, 36(12):743–748, 2013.

[6] Bernard De Bruyne, Nico H.J. Pijls, Bindu Kalesan, Emanuele Barbato, Pim A.L. Tonino, Zsolt Piroth, Nikola Jagic, Sven Möbius-Winkler, Gilles Rioufol, Nils Witt, Petr Kala, Philip MacCarthy, Thomas Engstrom, Keith G. Oldroyd, Kreton Mavromatis, Ganesh Manoharan,

Peter Verlee, Ole Frobert, Nick Curzen, Jane B. Johnson, Peter Jüni, and William F. Fearon. Fractional flow reserve-guided pci versus medical therapy in stable coronary disease. *New England Journal of Medicine*, 367(11):991–1001, 2012. PMID: 22924638.

[7] Nico H.J. Pijls, Bernard de Bruyne, Kathinka Peels, Pepijn H. van der Voort, Hans J.R.M. Bonnier, Jozef Bartunek, and Jacques J. Koolen. Measurement of fractional flow reserve to assess the functional severity of coronary-artery stenoses. *New England Journal of Medicine*, 334(26):1703–1708, 1996. PMID: 8637515.

[8] Pim A.L. Tonino, Bernard De Bruyne, Nico H.J. Pijls, Uwe Siebert, Fumiaki Ikeno, Marcel van 't Veer, Volker Klauss, Ganesh Manoharan, Thomas EngstrÃ¸m, Keith G. Oldroyd, Peter N. Ver Lee, Philip A. MacCarthy, and William F. Fearon. Fractional flow reserve versus angiography for guiding percutaneous coronary intervention. *New England Journal of Medicine*, 360(3):213–224, 2009. PMID: 19144937.

[9] Pamela S. Douglas, , Gianluca Pontone, , Mark A. Hlatky, , Manesh R. Patel, , Bjarne L. Norgaard, , Robert A. Byrne, , Nick Curzen, , Ian Purcell, , Matthias Gutberlet, , Gilles Rioufol, , Ulrich Hink, , Herwig Walter Schuchlenz, , Gudrun Feuchtner, , Martine Gilard, , Daniele Andreini, , Jesper M. Jensen, , Martin Hadamitzky, , and et al. Clinical outcomes of fractional flow reserve by computed tomographic angiography-guided diagnostic strategies vs. usual care in patients with suspected coronary artery disease: the prospective longitudinal trial of ffrct: outcome and resource impacts study. *European Heart Journal*, 36(47):3359, 2015.

[10] Medtronic. `http://www.medtronic.com/us-en/patients/treatments-therapies/heart-surgery-cad/know-your-arteries.html`, 2017. [Online; accessed 18.05.17].

[11] Arthur C. Guyton and John E. Hall. *Guyton and Hall textbook of medical physiology*, chapter 22, pages 246–257. Philadelphia, PA: Saunders, 2011.

[12] Brian R. Weil and John M. Canty. *Coronary Blood Flow and Myocardial Ischemia*, chapter 22, pages 387–403. Springer New York, New York, NY, 2013.

[13] Charles A. Taylor, Timothy A. Fonte, and James K. Min. Computational fluid dynamics applied to cardiac computed tomography for noninvasive quantification of fractional flow reserve: Scientific basis. *Journal of the American College of Cardiology*, 61(22):2233 – 2241, 2013.

[14] Inc. Vator. The top 15 healthcare deals of 2016. `http://vator.tv/news/2016-11-03-the-top-15-healthcare-deals-of-2016`, 2016. [Online; accessed 18.05.17].

[15] Bjarne L. Noergaard, Jonathon Leipsic, Sara Gaur, Sujith Seneviratne, Brian S. Ko, Hiroshi Ito, Jesper M. Jensen, Laura Mauri, Bernard De Bruyne, Hiram Bezerra, Kazuhiro Osawa, Mohamed Marwan, Christoph Naber, Andrejs Erglis, Seung-Jung Park, Evald H. Christiansen, Anne Kaltoft, Jens F. Lassen, Hans Erik BÃ¸tker, and Stephan Achenbach. Diagnostic performance of noninvasive fractional flow reserve derived from coronaryÂ computed tomography angiography in suspected coronary artery disease: The {NXT} trial (analysis of coronary blood flow using {CT} angiography: Next steps). *Journal of the American College of Cardiology*, 63(12):1145 – 1155, 2014.

[16] Paul D. Morris, Desmond Ryan, Allison C. Morton, Richard Lycett, Patricia V. Lawford, D. Rodney Hose, and Julian P. Gunn. Virtual fractional flow reserve from coronary angiography: Modeling the significance of coronary lesions: Results from the virtu-1 (virtual fractional flow reserve from coronary angiography) study. *JACC: Cardiovascular Interventions*, 6(2):149 – 157, 2013.

[17] Shengxian Tu, Emanuele Barbato, Zsolt Köszegi, Junqing Yang, Zhonghua Sun, Niels R. Holm, Balázs Tar, Yingguang Li, Dan Rusinaru, William Wijns, and Johan H.C. Reiber. Fractional flow reserve calculation from 3-dimensional quantitative coronary angiography and timi frame count: A fast computer model to quantify the functional significance of moderately obstructed coronary arteries. *JACC: Cardiovascular Interventions*, 7(7):768 – 777, 2014.

[18] Jun-Mei Zhang, Liang Zhong, Tong Luo, Aileen Mae Lomarda, Yunlong Huo, Jonathan Yap, Soo Teik Lim, Ru San Tan, Aaron Sung Lung Wong, Jack Wei Chieh Tan, Khung Keong Yeo, Jiang Ming Fam, Felix Yung Jih Keng, Min Wan, Boyang Su, Xiaodan Zhao, John Carson Allen, Ghassan S. Kassab, Terrance Siang Jin Chua, and Swee Yaw Tan. Simplified models of non-invasive fractional flow reserve based on ct images. *PLOS ONE*, 11(5):1–20, 05 2016.

[19] Yunlong Huo, Mark Svendsen, Jenny Susana Choy, Z.-D. Zhang, and Ghassan S. Kassab. A validated predictive model of coronary fractional flow reserve. *Journal of The Royal Society Interface*, 9(71):1325–1338, 2012.

[20] R E Mates, R L Gupta, A C Bell, and F J Klocke. Fluid dynamics of coronary artery stenosis. *Circulation Research*, 42(1):152–162, 1978.

[21] C.A. Bulant, P.J. Blanco, G.D. Maso Talou, C. Guedes Bezerra, P.A. Lemos, and R.A. Feijóo. A head-to-head comparison between ct- and ivus-derived coronary blood flow models. *Journal of Biomechanics*, 51:65 – 76, 2017.

[22] M. Zamir. *The Physics of Coronary Blood Flow*. Springer, 2005.

[23] Nicolaas Westerhof, Nikolaos Stergiopulos, and Mark I.M. Noble. *Snapshots of Hemodynamics*. Springer New York, 2010.

[24] Donald F. Young and Frank Y. Tsai. Flow characteristics in models of arterial stenoses - i. steady flow. *Journal of Biomechanics*, 6(4):395 – 410, 1973.

[25] Shingo Sakamoto, Saeko Takahashi, Ahmet U. Coskun, Michail I. Papafaklis, Akihiko Takahashi, Shigeru Saito, Peter H. Stone, and Charles L. Feldman. Relation of distribution of coronary blood flow volume to coronary artery dominance. *The American Journal of Cardiology*, 111(10):1420 – 1424, 2013.

[26] Ananda R. Jayaweera, Kevin Wei, Matthew Coggins, Jiang Ping Bin, Craig Goodman, and Sanjiv Kaul. Role of capillaries in determining cbf reserve: new insights using myocardial contrast echocardiography. *American Journal of Physiology - Heart and Circulatory Physiology*, 277(6):H2363–H2372, 1999.

[27] R F Wilson, K Wyche, B V Christensen, S Zimmer, and D D Laxson. Effects of adenosine on human coronary arterial circulation. *Circulation*, 82(5):1595–1606, 1990.

[28] Elizabeth O. Ofili, Arthur J. Labovitz, and Morton J. Kern. Coronary flow velocity dynamics in normal and diseased arteries. *The American Journal of Cardiology*, 71(14):D3 – D9, 1993.

[29] Morton J. Kern, Ubeydullah Deligonul, Satyanarayana Tatineni, Harvey Serota, Frank Aguirre, and Thomas C. Hilton. Intravenous adenosine: Continuous infusion and low dose bolus administration for determination of coronary vasodilator reserve in patients with and without coronary artery disease. *Journal of the American College of Cardiology*, 18(3):718 – 729, 1991.

[30] James D. Rossen, James E. Quillen, J.Antonio G. Lopez, Robert G. Stenberg, Charlotte L. Talman, and Michael D. Winniford. Comparison of coronary vasodilation with intravenous dipyridamole and adenosine. *Journal of the American College of Cardiology*, 18(2):485 – 491, 1991.

[31] Wikipedia. Claude-louis navier — Wikipedia, the free encyclopedia. `https://en.wikipedia.org/wiki/Claude-Louis_Navier`. [Online; accessed 20.05.17].

[32] Wikipedia. Sir george stokes, 1st baronet — Wikipedia, the free encyclopedia. `https://en.wikipedia.org/wiki/Sir_George_Stokes,_1st_Baronet`. [Online; accessed 20.05.17].

[33] Charles L. Fefferman. Existence and smoothness of the navier-stokes equation. http://www.claymath.org/sites/default/files/navierstokes.pdf. [Online; accessed 20.05.17].

[34] Jean Donea and Antonio Huerta. *Finite Element Method for Flow Problems*. Wiley, 2003.

[35] Wikipedia. Jean léonard marie poiseuille — Wikipedia, the free encyclopedia. https://en.wikipedia.org/wiki/Jean_L%C3%A9onard_Marie_Poiseuille. [Online; accessed 20.05.17].

[36] O. C. Zienkiewicz, Perumal Nithiarasu, and Robert L. Taylor. *The Finite Element Method for Fluid Dynamics.*, volume Seventh edition. Butterworth-Heinemann, 2014.

[37] Joaquim Peiró and Alessandro Veneziani. *Cardiovascular Mathematics: Modeling and Simulation of the Circulatory System*, chapter 2, pages 347–394. Springer, 2009.

[38] Kristian Valen-Sendstad, Anders Logg, Kent-Andre Mardal, Harish Narayanan, and Mikael Mortensen. *A comparison of finite element schemes for the incompressible Navier–Stokes equations*, pages 399–420. Springer Berlin Heidelberg, Berlin, Heidelberg, 2012.

[39] Øyvind Evju. *Sensitivity Analysis of Simulated Blood Flow in Cerebral Aneurysms*. PhD thesis, Universitetet i Oslo (UiO), 2011.

[40] Anders Logg, Kent-Andre Mardal, Garth N. Wells, et al. *Automated Solution of Differential Equations by the Finite Element Method*. Springer, 2012.

[41] John F Wendt, JD Anderson, G Degrez, E Dick, and R Grundmann. *Computational Fluid Dynamics*. Springer-Verlag, 1991.

[42] Wikipedia. Osborne reynolds — Wikipedia, the free encyclopedia. https://en.wikipedia.org/wiki/Osborne_Reynolds. [Online; accessed 20.05.17].

[43] Yunus A. Çengel and John M. Cimbala. *Fluid Mechanics: Fundamentals and Applications*. McGraw-Hill, 2010.

[44] Joaquim Peiró and Alessandro Veneziani. *Cardiovascular Mathematics: Modeling and Simulation of the Circulatory System*. Springer, 2009.

[45] Wikipedia. John r. womersley — Wikipedia, the free encyclopedia. https://en.wikipedia.org/wiki/John_R._Womersley. [Online; accessed 20.05.17].

[46] Catherine Loudon and Antoinette Tordesillas. The use of the dimensionless womersley number to characterize the unsteady nature of internal flow. *Journal of Theoretical Biology*, 191(1):63 – 78, 1998.

[47] Joaquim Peiró and Alessandro Veneziani. *Cardiovascular Mathematics: Modeling and Simulation of the Circulatory System*, chapter 10, pages 347–394. Springer, 2009.

[48] S. Mantero, R. Pietrabissa, and R. Fumero. The coronary bed and its role in the cardiovascular system: a review and an introductory single-branch model. *Journal of Biomedical Engineering*, 14(2):109 – 116, 1992.

[49] Johannes Kløve Kjernlie and Hallvard Moian Nydal. Closing the gap between reality and cfd simulations of ffr with techniques to quantify and reduce uncertainty of predictions. Master's thesis, Norwegian University of Science and Technology, 2016.

[50] Paul D. Morris, Frans N. van de Vosse, Patricia V. Lawford, D. Rodney Hose, and Julian P. Gunn. "virtual" (computed) fractional flow reserve: Current challenges and limitations. *JACC: Cardiovascular Interventions*, 8(8):1009–1017, 2015.

[51] Joaquim Peiró and Alessandro Veneziani. *Cardiovascular Mathematics: Modeling and Simulation of the Circulatory System*, chapter 11, pages 347–394. Springer, 2009.

[52] Espen Holte, Johnny Vegsundvaag, Knut Hegbom, Torstein Hole, and Rune Wiseth. Transthoracic doppler echocardiography for detection of stenoses in the left coronary artery byÂ use of poststenotic coronary flow profiles: comparison with quantitative coronary angiography and coronary flow reserve. *Journal of the American Society of Echocardiography*, 26(1):77 – 85, 2013.

[53] C. D. Murray. The Physiological Principle of Minimum Work. I. The Vascular System and the Cost of Blood Volume. *Proceedings of the National Academy of Science*, 12:207–214, March 1926.

[54] Lucian Mihai Itu, Puneet Sharma, Viorel Mihalef, Ali Kamen, Constantin Suciu, and Dorm Lomaniciu. A patient-specific reduced-order model for coronary circulation. In *ISBI*, 2012.

[55] Monique Troebs, Stephan Achenbach, Jens RÃ¶ther, Thomas Redel, Michael Scheuering, David Winneberger, Klaus Klingenbeck, Lucian Itu, Tiziano Passerini, Ali Kamen, Puneet Sharma, Dorin Comaniciu, and Christian Schlundt. Comparison of fractional flow reserve based on computational fluid dynamics modeling using coronary angiographic vessel morphology versus invasively measured fractional flow reserve. *The American Journal of Cardiology*, 117(1):29 – 35, 2016.

[56] Mette S. Olufsen. Structured tree outflow condition for blood flow in larger systemic arteries. *American Journal of Physiology - Heart and Circulatory Physiology*, 276(1):H257–H268, 1999.

[57] MA. Changizi and C. Cherniac. Modeling the large scale geometry of human coronary arteries. *Canadian Journal of Physiology and Pharmacology*, 2000.

[58] Carlos Alberto Bulant. Computational models for the geometric and functional assessment og the coronary circulation.

[59] Python. `https://www.python.org/`, 2017. [Online; accessed 07.06.17].

[60] L. Antiga and S. Manini. The vascular modeling toolkit. `http://www.vmtk.org/`, 2017. [Online; accessed 27.05.17].

[61] Martin S. Alnæs, Jan Blechta, Johan Hake, August Johansson, Benjamin Kehlet, Anders Logg, Chris Richardson, Johannes Ring, Marie E. Rognes, and Garth N. Wells. The fenics project version 1.5. *Archive of Numerical Software*, 3(100), 2015.

[62] Evju, M. S. Alnæs, K. Mardal, and K. Valen-Senstad. cbcflow. `https://bitbucket.org/simula_cbc/cbcflow.git`, 2016. [Online; accessed 27.05.17].

[63] Kitware. Paraview. `https://www.paraview.org/`, 2016. [Online; accessed 27.05.17].

[64] Katuhiko Goda. A multistep technique with implicit difference schemes for calculating two- or three-dimensional cavity flows. *Journal of Computational Physics*, 30(1):76 – 95, 1979.

[65] H. J. Kim, I. E. Vignon-Clementel, J. S. Coogan, C. A. Figueroa, K. E. Jansen, and C. A. Taylor. Patient-specific modeling of blood flow and pressure in human coronary arteries. *Annals of Biomedical Engineering*, 38(10):3195–3209, 2010.

[66] scikit-image. `http://scikit-image.org/`, 2017. [Online; accessed 27.05.17].

[67] Nornadiah Mohd Razali and Yap Bee Wah. Power comparisons of shapiro-wilk, kolmogorov-smirnov, lilliefors and anderson-darling tests. 2011.

[68] Scipy stats. `https://docs.scipy.org/doc/scipy/reference/stats.html`, 2017. [Online; accessed 06.06.17].

[69] Wikiecho. Doppler physics. `http://www.wikiecho.org/wiki/Doppler_Physics`. [Online; accessed 27.05.17].

[70] H.J. Kim, I.E. Vignon-Clementel, C.A. Figueroa, K.E. Jansen, and C.A. Taylor. Developing computational methods for three-dimensional finite element simulations of coronary blood flow. *Finite Elements in Analysis and Design*, 46(6):514 – 525, 2010. The Twenty-First Annual Robert J. Melosh Competition.

[71] Moloy Kumar Banerjee, Ranjan Ganguly, and Amitava Datta. Effect of pulsatile flow waveform and womersley number on the flow in stenosed arterial geometry. *ISRN Biomathematics, vol. 2012*, 2012.

[72] Carmel M. McEniery, Yasmin, Barry McDonnell, Margaret Munnery, Sharon M. Wallace, Chloe V. Rowe, John R. Cockcroft, and Ian B. Wilkinson. Central pressure: Variability and impact of cardiovascular risk factors. *Hypertension*, 51(6):1476–1482, 2008.

[73] Allen Jeremias, Robert J. Whitbourn, Steven D. Filardo, Peter J. Fitzgerald, David J. Cohen, E.Murat Tuzcu, William D. Anderson, Alexandre A. Abizaid, Gary S. Mintz, Alan C. Yeung, Morton J. Kern, and Paul G. Yock. Adequacy of intracoronary versus intravenous adenosine-induced maximal coronary hyperemia for fractional flow reserve measurements. *American Heart Journal*, 140(4):651 – 657, 2000.

[74] J. R. Womersley. Method for the calculation of velocity, rate of flow and viscous drag in arteries when the pressure gradient is known. *The Journal of Physiology*, 127(3):553–563, 1955.

[75] Morton J. Kern, Amir Lerman, Jan-Willen Bech, Bernard De Bruyne, Eric Eeckhout, William F. Fearon, Stuart T. Higano, Michael J. Lim, Martijn Meuwissen, Jan J. Piek, Nico H.J. Pijls, Maria Siebes, and Jos A.E. Spaan. Physiological assessment of coronary artery disease in the cardiac catheterization laboratory. *Circulation*, 114(12):1321–1341, 2006.

[76] Bernard de Bruyne, Jozef Bartunek, Stanislas U. Sys, Nico H.J. Pijls, Guy R. Heyndrickx, and William Wijns. Simultaneous coronary pressure and flow velocity measurements in humans. *Circulation*, 94(8):1842–1849, 1996.

[77] M. Malvè, A. García, J. Ohayon, and M.A. Martínez. Unsteady blood flow and mass transfer of a human left coronary artery bifurcation: {FSI} vs. {CFD}. *International Communications in Heat and Mass Transfer*, 39(6):745 – 751, 2012.

[78] Colin Berry, Marcel van 't Veer, Nils Witt, Petr Kala, Otakar Bocek, Stylianos A. Pyxaras, John D. McClure, William F. Fearon, Emanuele Barbato, Pim A.L. Tonino, Bernard De Bruyne, Nico H.J. Pijls, and Keith G. Oldroyd. {VERIFY} (verification of instantaneous wave-free ratio and fractional flow reserve for the assessment of coronary artery stenosis

severity in everyday practice): A multicenter study in consecutive patients. *Journal of the American College of Cardiology*, 61(13):1421 – 1427, 2013.

[79] Jenny Susana Choy and Ghassan S. Kassab. Scaling of myocardial mass to flow and morphometry of coronary arteries. *Journal of Applied Physiology*, 104(5):1281–1286, 2008.

[80] Stig Marsteng Nilsen. Numeriske bereginger av blodstrømning for diagnostisering av koronarsykdom. Master's thesis, Norwegian University of Science and Technology, 2016.

[81] Nils P. Johnson, Daniel T. Johnson, Richard L. Kirkeeide, Colin Berry, Bernard De Bruyne, William F. Fearon, Keith G. Oldroyd, Nico H.J. Pijls, and K. Lance Gould. Repeatability of fractional flow reserve despite variations in systemic and coronary hemodynamics. *JACC: Cardiovascular Interventions*, 8(8):1018–1027, 2015.

A

Derivation of FFR

The clinically applied definition of FFR is

$$FFR = \frac{P_d}{P_p}, \tag{A.1}$$

where P_d is the pressure distal (downstream) to a stenosis, and P_p is the proximal pressure, equal to the aortic pressure P_{ao} by convention. FFR is however essentially based on the ratio of volumetric coronary blood flow in the presence of a stenosis to the hypothetic flow in a healthy artery:

$$FFR = \frac{Q_s}{Q_h} \tag{A.2}$$

Q_s is the stenotic flow, and Q_h is the possible flow in a healthy vessel. Applying that $Q = \Delta P/R$, (A.2) can be rewritten as

$$FFR = \frac{\Delta P_s R_h}{\Delta P_h R_s} \tag{A.3}$$

Where $\Delta P_s = P_d - P_v$ is the pressure drop from distal of the stenosis, to the venous pressure. $\Delta P_h = P_{ao} - P_v$, assuming that the pressure drop from the aorta to the distal location in the healthy coronary artery is negligible. Further assuming that $R_h = R_s$, meaning that the peripheral resistance is not affected by the stenosis, (A.3) becomes:

$$FFR = \frac{P_d - P_v}{P_{ao} - P_v} \tag{A.4}$$

Finally, neglecting the venous pressure being much smaller than arterial pressures, one arrives at (A.1).

Q.E.D.

B

Coronary0D Code

```
#####################################################
# Get solution for the cor-0D model from input curves (P_aorta or Q_LM) as inlet BC and the left ventricle (LV) pressure curve.
#
# Cor-0D model [1]:
#
#            R_p P_a R_m P_m R_d
#         .--mmm--.--mmm--.--mmm---P_d
#   ~P_in-|       |       |
#     or -|       = C_a   = C_m
#   ~Q_in-|       |       |
#         |       |      ~P_LV
#         V       V       |
#                         V
#
#     ~:    input curve
#     .:    pressure location
#    mmm:   resistance
#     =:    capacitor
#     V:    ground
#     Q_x is the flow through R_x
#
# [1] Mantero et al. (1992), The coronary bed and its role in the cardiovascular system: a review and an introductory single-branch
```

```
    model
#
##################################################

import numpy as np
import os
import ConfigParser
import matplotlib.pyplot as plt
from scipy import interpolate
import csv
import seaborn as sns
from sympy.physics.units import Pa
from pdb import pm

##################################################
## Parameters to be modified

T = 0.8 # Period [s]
N = 50 # Set higher if solution is not the steady
dt = 0.001
inletType = ’Q’ # ’P’ or ’Q’
write = False
outputFileName = ’output_filename.out’ # Output pressure or flow

# Patient specific (all units are in the cgs-system):
Rtot = 41942.1561888512 # Total coronary resistance
Ctot = 0.00004203    # Total coronary compliance
LVTarget = 153320.3 # Left ventricle maximal pressure target (SBP)
PaoAvgTarget = 117723.33 # Average aortic pressure target (MAP)
PaoPulseTarget = 53328.80 # Aortic pulse pressure target (PP)
inflowAvgTarget = 1.6666667 # Inlet flow targe (Q)

## Data input curves (format: [time pressure])
LVData = np.genfromtxt(’path/to/LV_pressure_curve’)
PaoData = np.genfromtxt(’path/to/aortic_pressure_curve’)
qLMData = np.genfromtxt(’path/to/inlet_flow_curve’)

##################################################

## Distribution of parameters:
R_p = 0.35*Rtot
R_m = 0.5*Rtot
R_d = 0.15*Rtot
C_a = 0.1*Ctot
C_m = 0.9*Ctot

```

```
# Set period = T
LVData[:,0] *= T
# LV Pressure
LVData[:,1] *= LVTarget
tC = np.linspace(0,T,100)
vNumpy = np.interp(tC, LVData[:,0], LVData[:,1],period=LVData[-1,0])
LVfun = interpolate.interp1d(tC,vNumpy,kind='cubic')

## Compute inlet
def compInletCurve(data,inletAverageTarget,inletPulseTarget=0,P=True):
    n_points = data.shape[0]
    Ta = data[-1,0] - data[0,0]
    integral = 0.
    for i in range(n_points-1):
        integral += (data[i+1,0]-data[i,0])*0.5*(data[i+1,1]+data[i,1])
    # Rescale time to match specified perior
    integral /= Ta
    timeD = (data[:,0] - data[0,0])/Ta*T
    if P==True:
        flowD = data[:,1]/integral
        flowD -= flowD.min()
        flowD = flowD/flowD.max()*inletPulseTarget
        avg = np.sum(flowD)/flowD.shape[0]
        flowD -= avg
        flowD += inletAverageTarget
    else:
        flowD = data[:,1]*inletAverageTarget/integral

    vNumpy = np.interp(tC, timeD, flowD,period=timeD[-1])
    return interpolate.interp1d(tC,vNumpy,kind='cubic')

PaoFun = compInletCurve(PaoData,PaoAvgTarget, PaoPulseTarget)
QinFun = compInletCurve(qLMData, inflowAvgTarget,P=False)

def dpdt(Q_ins,Q_outs,C):
    return ((Q_ins-Q_outs)/C)

## Initial conditions
P_a = 119989.8
P_d = 6666.1
P_p = P_a
P_m = P_a
P_LV = LVfun(0)
Q_in = 0.
V_m = (P_m - P_LV)/C_m
n = np.ceil(T/dt)
```

```
tn = np.linspace(0,T,np.ceil(T/dt))
dt = T/(len(tn))

Pp = np.array([])
Pa = np.array([])
Pm = np.array([])
Qd = np.array([])
Qp = np.array([])
Qm = np.array([])
ttot = np.array([])

## Solve with explicit Euler in time:
for period in range(N):
    for t in tn:
        # cor-0D BCs:
        P_LV = LVfun(t)
        if inletType == 'Q':
            Q_in = QinFun(t)
        elif inletType == 'P':
            P_p = PaoFun(t)
        else:
            print "Error: invalid inletType"

        # _X are next time step values
        _Q_in = Q_in
        _P_p = P_p

        # Explicit Euler method
        Q_m = (P_a-P_m)/R_m
        _P_a = P_a + dt*dpdt(Q_in,Q_m,C_a)
        Q_d = (P_m-P_d)/R_d

        _V_m = V_m + dt*(Q_m-Q_d)
        _P_m = _V_m/C_m + P_LV

        P_a = _P_a
        P_m = _P_m
        V_m = _V_m

        Q_d = (P_m-P_d)/R_d
        _P_p = P_a + Q_in*R_p
        _Q_in = (P_p-P_a)/R_p

        Q_in = _Q_in
        P_p = _P_p

```

```
        Pp = np.append(Pp,P_p)
        Pa = np.append(Pa,P_a)
        Pm = np.append(Pm,P_m)
        Qd = np.append(Qd,Q_d)
        Qp = np.append(Qp,Q_in)
        Qm = np.append(Qm,Q_m)
        ttot = np.append(ttot,period*T+t)

## Extract only n last cycles:
# The step response of the system is extremely compliant. Only the last n cycles should be saved (the periodic solution)

def getLastCycles(cycleData,noCycles):
    cycleData = cycleData[ttot>ttot[-1]-noCycles*T]
    return cycleData

noCyc = 1
Pp = getLastCycles(Pp,noCyc)
Pa = getLastCycles(Pa,noCyc)
Pm = getLastCycles(Pm,noCyc)
Qd = getLastCycles(Qd,noCyc)
Qp = getLastCycles(Qp,noCyc)
Qm = getLastCycles(Qm,noCyc)
ttot = ttot[ttot>ttot[-1]-noCyc*T]
ttot = ttot - min(ttot)

## Plotting
plt.figure()
plt.subplot(211)
plt.title('Inlet curve is %s' % (inletType))
plt.plot(ttot,np.divide(Pp,1333.22), label='P_p')
# Plot internal model pressures:
#plt.plot(ttot,np.divide(Pa,1333.22), label='P_a')
#plt.plot(ttot,np.divide(Pm,1333.22), label='P_m')
plt.legend(loc='upper right')
# Set one x-tick every cycle:
plt.xticks(np.arange(round(min(ttot),0), max(ttot)+T, T))
plt.subplot(212)
plt.plot(ttot,Qp, label='Q_in')
# Plot internal model flows:
#plt.plot(ttot,Qm, label='Q_m')
#plt.plot(ttot,Qd, label='Q_d')
plt.legend(loc='upper right')
# Set one x-tick every cycle:
plt.xticks(np.arange(round(min(ttot),0), max(ttot)+T, T))
plt.show()
```

```

## Write output data to file
if write == True:
    if inletType == 'P':
        nd = np.column_stack((ttot,Qp))
    else:
        nd = np.column_stack((ttot,Pp))
    # Write to file
    with open(outputFileName,'wb') as f:
        for line in nd:
            f.write("%15.9f %15.9f\n" % (line[0], line[1]/1333.22))
        f.close
```